ISSN 2409-5613 (print)
ISSN 2411-1414 (online)

Chimica Techno Acta

2019. Vol. 6. N 2

cta.urfu.ru

Editorial Board

Editor-in-Chief

A. Yu. Zuev (Ekaterinburg, Russia)

Managing Editor

T. A. Pospelova (Ekaterinburg, Russia)

Copyeditor

V. V. Sereda (Ekaterinburg, Russia)

Editors

E. V. Antipov (Moscow, Russia)
V. A. Cherepanov (Ekaterinburg, Russia)
Zh.-J. Fan (Tianjin, China)
V. V. Gusarov (Saint Petersburg, Russia)
V. V. Kharton (Chernogolovka, Russia)
A. A. Mikhailovsky (Santa Barbara, United States)
V. V. Pankov (Minsk, Belarus)
Sougata Santra (Ekaterinburg, Russia)
N. V. Tarakina (Berlin, Germany)
G. V. Zyryanov (Ekaterinburg, Russia)
D. A. Medvedev (Ekaterinburg, Russia)
P. Tsiakaras (Thessaly, Greece)
S. Song (Guangzhou, China)
Y. Wang (Guangzhou, China)

Редакционный совет

Главный редактор

А. Ю. Зуев (Екатеринбург, Россия)

Зав. редакцией

Т. А. Поспелова (Екатеринбург, Россия)

Научный редактор

В. В. Середа (Екатеринбург, Россия)

Редакторы

Е. В. Антипов (Москва, Россия)
В. А. Черепанов (Екатеринбург, Россия)
Ж.-Дж. Фан (Тяньцзинь, Китай)
В. В. Гусаров (Санкт-Петербург, Россия)
В. В. Хартон (Черноголовка, Россия)
А. А. Михайловский (Санта-Барбара, США)
В. В. Паньков (Минск, Беларусь)
Согата Сантра (Екатеринбург, Россия)
Н. В. Таракина (Берлин, Германия)
Г. В. Зырянов (Екатеринбург, Россия)
Д. А. Медведев (Екатеринбург, Россия)
П. Циакарас (Фессалия, Греция)
С. Сонг (Гуанчжоу, Китай)
Й. Ванг (Гуанчжоу, Китай)

Chimica Techno Acta

2019 | Vol. 6 | № 2

Scientific and Technical Journal
Established in 2014
Published four times per year

Chimica Techno Acta
© Ural Federal University, 2019

Founded by Ural Federal University named after the first President of Russia B. N. Yeltsin
19, Mira St., Ekaterinburg, 620002, Russia

Chimica Techno Acta

2019 | Vol. 6 | № 2

Научно-технический журнал
Журнал основан в 2014 г.
Выходит четыре раза в год

Chimica Techno Acta
© Уральский федеральный университет, 2019

Учредитель — Уральский федеральный университет имени первого Президента России Б. Н. Ельцина
620002, Россия, Екатеринбург, ул. Мира, 19

Graphical Abstracts

CONTENTS/СОДЕРЖАНИЕ

Vdovin G. K., Rudenko A. O., Antonov B. D.,
Malkov V. B., Demin A. K., Medvedev D. A.
Chimica Techno Acta. 2019. Vol. 6, No. 2. P. 38–45.
ISSN 2409–5613

DOI: 10.15826/chimtech.2019.6.2.01

G. K. Vdovin[a], A. O. Rudenko[a], B. D. Antonov[a], V. B. Malkov[a], A. K. Demin[ab], D. A. Medvedev[ab]

[a] *Institute of High Temperature Electrochemistry, Yekaterinburg 620990, Russia*
[b] *Graduate School of Economics and Management, Ural Federal University, Yekaterinburg 620002, Russia*
e-mail: dmitrymedv@mail.ru

Manipulating the grain boundary properties of $BaCeO_3$-based ceramic materials through sintering additives introduction

$BaCeO_3$-based materials represent a well-known family of proton-conducting electrolytes, which can be used in different solid oxide electrochemical devices. An effective operation of the latter across an intermediate-temperature range requires improved transport of PCEs, including their grain (G) and grain boundary (GB) components. In the present work, some 3d-elements in a small amount were used as sintering additives to verify the possibility of improving the GB conductivity of $BaCe_{0.9}Gd_{0.1}O_{3-\delta}$. It is shown that copper oxide (CuO) can be considered as one of the most effective sintering agents, since its use enables decreasing the GB density of the BCG ceramic material at the reduced sintering temperatures. The obtained results form a new tactic for designing new protonic electrolytes, whose conductivity might be prevail over ones containing Ni-based modifiers.

Keywords: $BaCeO_3$; SOFCs; SOECs; sintering additives; impedance spectroscopy; proton-conducting electrolytes.

Received: 11.06.2019. Accepted: 28.06.2019. Published: 05.08.2019.

© Vdovin G. K., Rudenko A. O., Antonov B. D., Malkov V. B., Demin A. K., Medvedev D. A., 2019

Introduction

Proton-conducting oxide (PCO) materials occupy a special place in the high-temperature electrochemistry due to its unique features consisting in proton transportation in an oxide matrix [1–5]. These features allows PCOs to be utilized as electrolytes for various types of electrochemical devices (EDs) such as solid oxide fuel cells (SOFCs), solid oxide electrolysis cells (SOECs), pumps and sensors [6–9]. As a result of high realizable conductivity levels of PCOs, the mentioned devices can operate at reduced temperatures (below 600 °C) compared with the conventional systems based on oxygen-ionic electrolytes [10, 11].

In order to further improve the EDs' performance and efficiency, different strategies aimed at the electrolyte modifications can be exploited [1–3, 12–14]: the decrease of their thickness, designing the structures with a higher ionic mobility, purposeful modification of ceramics morphology. The latter is a highly promising strategy, since the overall conductivity of polycrystalline PCOs is known to be determined by a high resistance of grain boundaries [14]. One of the most obvious

ways to modify the grain boundaries rests on adding the low-melting phases [15], which intensify mass transport and promotes grain growth. Nickel oxide (NiO) is often used as such an additive. However, no improvement (or even deterioration) of grain boundary transport is observed [16–20]; this is due to two undesirable effects: very low solubility of Ni^{2+}-ions in a Ce-sublattice of $BaCeO_3$-based materials and, consequently, the sedimentation of proton-blocking Ni-containing phases (NiO, BaY_2NiO_5) along the grain boundaries. Therefore, a rational search of possible alternative to NiO is a matter of fundamental and applied interests associated, respectively, with design of PCOs with optimized properties and their successful application in EDs.

In the present work, on a well-known example of PCOs, $BaCe_{0.9}Gd_{0.1}O_{3-\delta}$, possibility of improving its grain boundary transport was checked via an addition of CuO, Co_3O_4 and NiO as second dopants. To launch bridges between structural, microstructural and transport properties of the materials obtained, the X-ray diffraction (XRD), scanning electron microscopy (SEM) and electrochemical impedance spectroscopy (EIS) analyses were used.

Experimental

$BaCe_{0.9}Gd_{0.1}O_{3-\delta}$ (BCG) material and its doping derivatives ($BaCe_{0.89}Gd_{0.1}M_{0.01}O_{3-\delta}$, BCGM, where M = Cu, Co and Ni) were prepared using traditional solid state synthesis method. $BaCO_3$, CeO_2, Gd_2O_3, CuO, Co_3O_4 and NiO powders (with purity not less than 99.5%) were taken in stoichiometric amounts and thoroughly mixed via a mortar and pestle. The obtained mixtures were first pre-synthesized at 1100 °C for 5 h. The resulting powders were again mechanically activated, uniaxally pressed into discs and then sintered at 1450 °C for 3 h.

One part of the obtained ceramic samples was crushed and characterized by XRD (diffractometer Rigaku D/MAX-2200VL/PC, Japan), while another part was studied by SEM (JEOL JSM-5900 LV, Japan).

Electrochemical characterization was performed for the Ag|BCG|Ag or Ag|BCGM|Ag symmetrical cells by utilizing an Amel 2550 potentiostat/galvanostat (Italy) and a MaterialsM 520 frequency response analyser (Italy). These cells were fabricated in the following sequence: polishing the discs, an Ag paste painting and its sintering at 800 °C for 1 h. The impedance spectra were obtained for wet (pH_2O = 0.03 atm) air atmosphere in a frequency range of 10^{-2}–10^6 Hz with an amplitude of 30 mV. The spectra were analysed by an equivalent circuit method, using a ZView software for model processing.

Results and discussion

The XRD pattern of the sintered BCG material (Fig. 1) shows the formation of a single-phase product, the crystal structure of which can be indexed as an orthorhombically-distorted perovskite with lattice parameters of a = 6.221 Å, b = 8.770 Å, c = 6.244 Å and space group of *Pmcn*. The doping with 3d-elements does not change symmetry of the perovskite structure, while the lattice parameters of BCGM are virtually constant (a = 6.220 ± 0.003 Å, b = 8.766 ± 0.005 Å, c = 6.237 ± 0.007 Å). These results can be explained by the extremely small amount of sintering additives introduced into the $BaCeO_3$ structure, 0.005 mol.%.

Despite of small concentrations used, the M-doping affects considerably the microstructural parameters of the sintered materials that can be seen from qualitative (Fig. 2) and quantitative (Table 1) analyses. In detail, the processes associated with grains growth, their close package, pores disappearance and densification occur in all the cases. Nevertheless, a degree of these processes is different and increases in the sequence of BCGCo–BCGCu–BCGNi, indicating dissimilar nature of the sintering additives.

To reveal grain ($\sigma_{g.}$) and grain boundary ($\sigma_{g.b.}$) contributions of the total conductivity (σ_{total}), the EIS analysis was successfully performed. The electrochemical characterization was carried out in different tem-

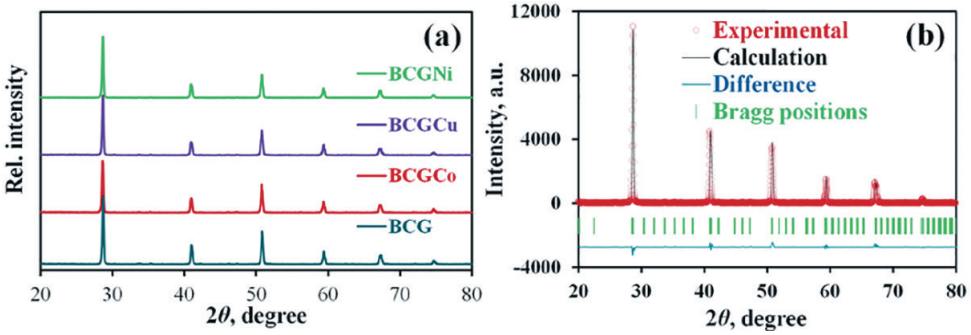

Fig. 1. XRD patterns of the sintered BCG and BCGM materials (a) and example of refinement for BCG (b)

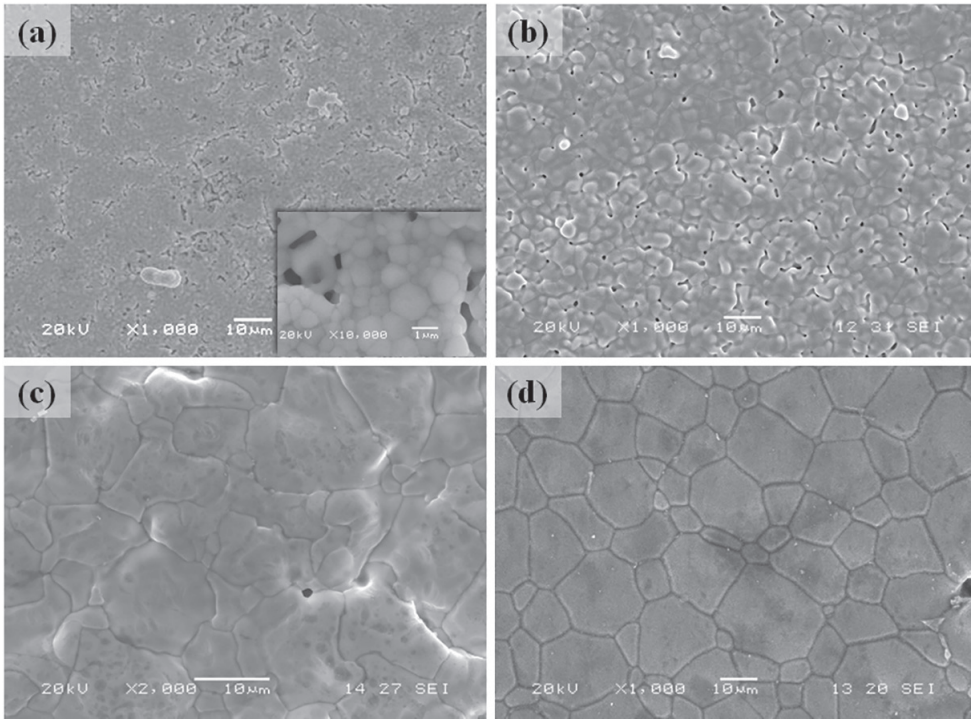

Fig. 2. Surface morphology of the sintered ceramic materials: BCG (a), BCGCo (b), BCGCu (c) and BCGNi (d)

Table 1

Microstructural parameters of the BCG and BCGM materials sintered at 1450 °C for 3 h: ρ is the relative density, *L* is the total shrinkage, *D* is the average grain size, γ is the grain boundary density [a]

Composition	ρ, %	*L*, %	*D* ± 5%, μm	γ ± 5%, μm^{-1}
BCG	86	8.2	0.8	4.66
BCGCo	91	12.3	3.4	1.10
BCGCu	94	17.5	6.9	0.54
BCGNi	97	22.3	9.6	0.39

[a] estimated on the base of the following equation: $\gamma = 3.722 \cdot D^{-1}$, see ref. [21].

perature ranges, boundaries of which were determined by accuracy of the analysis. The obtained spectra (Fig. 3) were analyzed using an equivalent circuit scheme of R_o–(R_1Q_1)–(R_2Q_2)–(R_3Q_3), where *R* is the resistance, *Q* is the constant phase element, indexes of 1, 2, 3 correspond to grain, grain boundary and electrode processes, respectively. Correlation of hodographs' elements with these processes is performed analyzing the characteristic capacitance (*C*) and frequency (*f*) values calculated as follows:

$$C = (R \cdot Q)^{1/n} \cdot R^{-1} \quad (1)$$

$$f = (R \cdot Q)^{-1/n} \cdot (2\pi)^{-1} \quad (2)$$

Here, *n* is the power index in a frequency dependence part of the constant phase element. Depending on the temperature, the *C* value varies between 20 and 80 pF for the first arc and between 3 and 8 nF for the second one, while the *f* values amount hundreds kHz and hundreds Hz, respectively. Both levels of these parameters relate with grain and grain boundary properties.

It should be noted that R_o = 0.001 Ω was purposefully introduced in the equivalent circuit scheme; it imitates the origin of the coordinates, providing a correct fitting.

As can be seen from Fig. 4a, Cu- and Ni-doping of BCG results in an increase of $\sigma_{g.}$, while Co-doping has an opposite (but minor) effect. For example, the $\sigma_{g.}$ value at 200 °C reaches $5.01 \cdot 10^{-5}$, $3.27 \cdot 10^{-5}$ and $2.61 \cdot 10^{-4}$ S cm^{-1} for BCG, BCGCo and BCGCu, respectively. This parameter cannot be precisely determined for the BCGNi material at 200 °C, but its $\sigma_{g.}$ level is by ~2 times lower than that of BCGCu at the lower temperatures (100–150 °C).

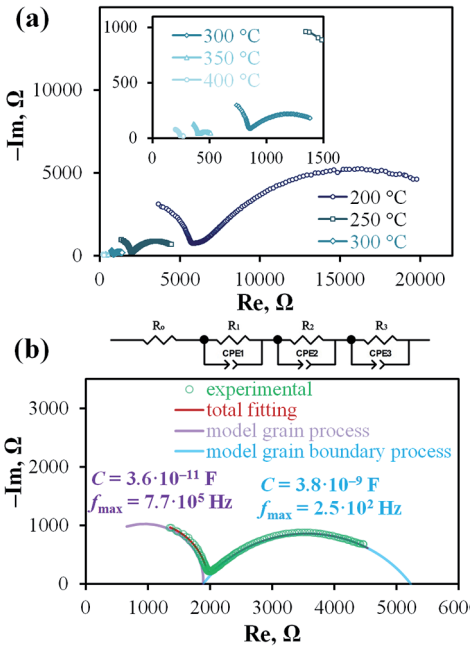

Fig. 3. Impedance spectra obtained for the Ag|BCG|Ag symmetrical cell at different temperatures in wet air atmosphere (a) and example of the fitting procedure for the spectra obtained at 250 °C (b)

Discussing the grain boundary transport (Fig. 4*b*), the $\sigma_{g.b.}$ improvement is observed for all the BCG-modified materials and can be related with decreasing the grain boundary density (Table 1). Comparison of the BCGCu and BCGNi samples allows formulation of the assumption that nickel is only partially dissolved in the Ce-sublattice of BCG, while another part localizes onto grain boundaries. This proposal is based on the fact that BCGNi exhibits the lowest grain boundary density, which should provide the highest $\sigma_{g.b.}$; however, this is not confirmed experimentally.

The resulting conductivity (σ_{total}, Fig. 4*c*) of the BCGM samples is higher than that of BCG, showing that the grain boundary transport determines the overall properties even for BCGCo (at least in the entire studied temperature range). The BCGCu material exhibits the maximal achievable σ_{total} values, ranging from $6.33 \cdot 10^{-6}$ S cm^{-1} at 100 °C to $1.86 \cdot 10^{-4}$ S cm^{-1} at 200 °C.

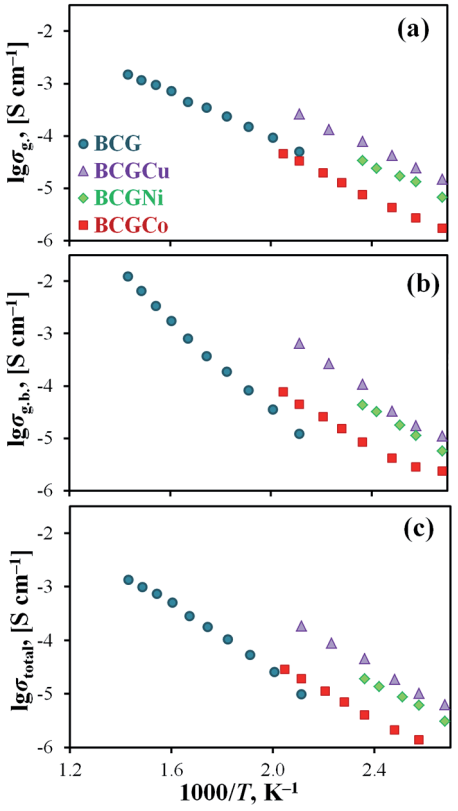

Fig. 4. Grain (a), grain boundary (b) and total (c) conductivities of the BCG and BCGM ceramic materials

As shown in Fig. 5, the apparent activation energies (E_a) of $\sigma_{g.}$ fall in the range of 0.45–0.49 eV, being in close agreement with a characteristic value of 0.5 eV for proton transportation of PCOs [22–24]. According to these data, the M-doping does not affect the grain transport properties of BCG. Another scenario is observed for the grain boundary transport properties, when E_a of $\sigma_{g.b.}$ decreases by 25–40% comparatively 0.92 eV reaching for the basic BCG oxide. It might be also associated with the meaningful decrease of grain boundary density serving as a barrier to ionic charge transfer.

Fig. 6 displays the most interesting result — a ratio between the grain boundary ($R_{g.b.}$) and total (R_{total}) resistances of BCG and BCGM. This ratio decreases significantly for the latter samples as a result of weakening the effect of grain boundaries on the overall transport of BCGM. A vivid example can be seen when $R_{g.b.}/R_{total}$ = = 0.5: for BCG this level is reached at ~250 °C, whereas for BCGM — at 100–125 °C. In terms of real operation of PCOs (400–600 °C), the introduction of 3d-elemetns in small amounts can improve the out-

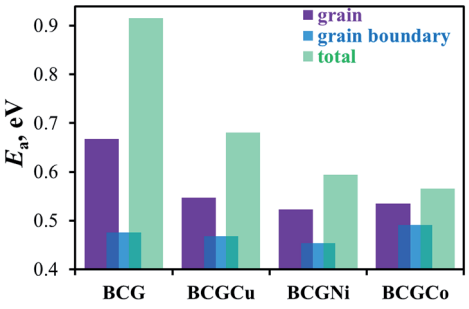

Fig. 5. Apparent activation energy values calculated for different types of conductivities

put properties (power density, current density) of PCO-based electrochemical devices by tens of percent.

Considering transport properties of BCGM and data on low-melting phases in corresponding systems [25–27], it can be concluded that the studied dopants behave differently respectively each other. For example, cobalt is assumed to act as a dopant, fully incorporated in the Ce-site of $BaCeO_3$; nickel is mostly localizes at grain boundary region due to the mentioned low solubility in the Ce-sublattice, although a certain amount can be nonetheless incorporated; finally, copper demonstrates dual nature: it has a high solubility (at least, more than 5 mol.% [21]), but can be also formed as a sediment at grain boundaries because of very low melting temperatures detected for a Ba–Cu–O system [15, 27].

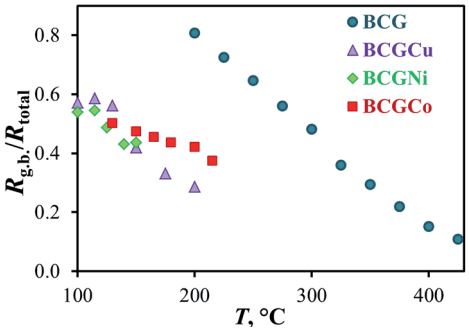

Fig. 6. Temperature dependence of grain boundary resistance contribution of the total resistance of the BCG and BCGM ceramic materials

Conclusions

This work shows that the doping strategy of barium cerate with transition elements is one of the simplest and most effective methods aimed at fabricating the gas-tight ceramic samples at reduced sintering temperatures. This effect is achieved due to the intensification of diffusion processes caused by the appearance of a liquid phase. The latter leads not only to an increase in the relative density of the ceramic materials, but also to grain size growth, which may be favorable for designing new polycrystalline materials and rational engineering their grain boundary parameters.

Acknowledgements

This study was performed within the framework of the Russian Science Foundation [grant no. 18-73-00001].

The characterization of powder and ceramic materials was carried out at the Shared Access Centre “Composition of Compounds” of the Institute of High Temperature Electrochemistry [28].

References

1. Meng Y, Gao J, Zhao Z, Amoroso J, Tong J, Brinkman KS. Review: recent progress in low-temperature proton-conducting ceramics. J Mater Sci. 2019;54(13):9291–312. DOI: 10.1007/s10853-019-03559-9.
2. Kim J, Sengodan S, Kim S, Kwon O, Bu Y, Kim G. Proton conducting oxides: A review of materials and applications for renewable energy conversion and storage. Renew Sustain Energy Rev. 2019;109:606–18 DOI: 10.1016/j.rser.2019.04.042.

3. Mohd Rashid NLR, Samat AA, Jais AA, Somalu MR, Muchtar A, Baharuddin NA, Wan Isahak WNR. Review on zirconate-cerate-based electrolytes for proton-conducting solid oxide fuel cell. Cerm Int. 2019;45(6)6605–15.
DOI: 10.1016/j.ceramint.2019.01.045.
4. Putilov LP, Tsidilkovski VI. Impact of bound ionic defects on the hydration of acceptor-doped proton-conducting perovskites. Phys Chem Chem Phys. 2019;21(12):6391–406.
DOI: 10.1039/C8CP07745B.
5. Wang W, Medvedev D, Shao Z. Gas humidification impact on the properties and performance of perovskite-type functional materials in proton-conducting solid oxide cell. Adv Funct Mater. 2018;28(48):1802592.
DOI: 10.1002/adfm.201802592.
6. Putilov LP, Demin AK, Tsidilkovski VI, Tsiakaras P. Theoretical modeling of the gas humidification effect on the characteristics of proton ceramic fuel cells. Appl Energy. 2019;242:1448–59.
DOI: 10.1016/j.apenergy.2019.03.096.
7. Tarutin A, Lyagaeva J, Farlenkov A, Plaksin S, Vdovin G, Demin A, Medvedev D. A reversible protonic ceramic cell with symmetrically designed $Pr_2NiO_{4+\delta}$-based electrodes: fabrication and electrochemical features. Materials. 2019;12(1):118.
DOI: 10.3390/ma12010118.
8. Danilov N, Lyagaeva J, Vdovin G, Medvedev D. Multifactor performance analysis of reversible solid oxide cells based on proton-conducting electrolytes. Appl Energy. 2019;237:924–34.
DOI: 10.1016/j.apenergy.2019.01.054.
9. Volkov A, Gorbova E, Vylkov A, Medvedev D, Demin A, Tsiakaras P. Design and applications of potentiometric sensors based on proton-conducting ceramic materials. A brief review. Sens Actuators B. 2017;244:1004–15.
DOI: 10.1016/j.snb.2017.01.097.
10. Dai H, Kou H, Wang H, Bi L. Electrochemical performance of protonic ceramic fuel cells with stable $BaZrO_3$-based electrolyte: A mini-review. Electrochem Commun. 2018;96:11–5.
DOI: 10.1016/j.elecom.2018.09.00.
11. Yang L, Wang S, Blinn K, Liu M, Liu Z, Cheng Z, Liu M. Enhanced sulfur and coking tolerance of a mixed ion conductor for SOFCs: $BaZr_{0.1}Ce_{0.7}Y_{0.2-x}Yb_xO_{3-\delta}$. Science. 2009;326(5949):126–9.
DOI: 10.1126/science.1174811.
12. Lee YH, Chang I, Cho GY, Park J, Yu W, Tanveer WH, Cha SW. Thin film solid oxide fuel cells operating below 600°C: a review. Int J Precis Eng Manuf. 2018;5(3):441–53.
DOI: 10.1007/s40684-018-0047-0.
13. Cho GY, Lee YH, Cha SW. Thin film process for thin film solid oxide fuel cells — a review. J Korean Soc Precis Eng. 2018;35(12):1119–29.
DOI: http://dx.doi.org/10.7736/KSPE.2018.35.12.1119.
14. Kjølseth C, Fjeld H, Prytz Ø, Dahl PI, Estournès C, Haugsrud R, Norby T. Space-charge theory applied to the grain boundary impedance of proton conducting $BaZr_{0.9}Y_{0.1}O_{3-\delta}$. Solid State Ionics. 2010;181(5–7):268–75.
DOI: 10.1016/j.ssi.2010.01.014.

15. German RM, Suri P, Park SJ. Review: liquid phase sintering. J Mater Sci. 2009;44(1):1–39. DOI: 10.1007/s10853-008-3008-0.
16. Tong J, Clark D, Bernau L, Subramaniyan A, O'Hayre R. Proton-conducting yttrium-doped barium cerate ceramics synthesized by a cost-effective solid-state reactive sintering method. Solid State Ionics. 2010;181(33–34):1486–98. DOI: 10.1016/j.ssi.2010.08.022.
17. Yun DS, Kim J, Kim S-J, Lee J-H, Kim J-N, Yoon HC, Yu JH, Kwak M, Yoon H, Cho Y, Yoo C-Y. Structural and electrochemical properties of dense yttria-doped barium zirconate prepared by solid-state reactive sintering. Energies. 2018;11(11):3083. DOI: 10.3390/en11113083.
18. Fang S, Wang S, Brinkman KS, Su Q, Wang H, Chen F. Relationship between fabrication method and chemical stability of Ni–$BaZr_{0.8}Y_{0.2}O_{3-\delta}$ membrane. J Power Sources. 2015;278:614–22. DOI: 10.1016/j.jpowsour.2014.12.108.
19. Narendar N, Mather GC, Diasa PAN, Fagg DP. The importance of phase purity in Ni–$BaZr_{0.85}Y_{0.15}O_{3-\delta}$ cermet anodes — novel nitrate-free combustion route and electrochemical study. RSC Adv. 2013;3(3):859–69. DOI: 10.1039/C2RA22301E.
20. Han D, Otani Y, Noda Y, Onishi T, Majima M, Uda T. Strategy to improve phase compatibility between proton conductive $BaZr_{0.8}Y_{0.2}O_{3-\delta}$ and nickel oxide. RSC Adv. 2016;6(23):19288–97. DOI: 10.1039/C5RA26947D.
21. Ananyev M, Medvedev D, Gavrilyuk A, Mitri S, Demin A, Malkov V, Tsiakaras P. Cu and Gd co-doped $BaCeO_3$ proton conductors: experimental vs SEM image algorithmic-segmentation results. Electrochim Acta. 2014;125:371–9. DOI: 10.1016/j.electacta.2013.12.161.
22. Kreuer KD. Proton-conducting oxides. Annu Rev Mater Res. 2003;33:333–59. DOI: 10.1146/annurev.matsci.33.022802.091825.
23. Malavasi L, Fisher CAJ, Islam MS. Oxide-ion and proton conducting electrolyte materials for clean energy applications: structural and mechanistic features. Chem Soc Rev. 2010;39(11):4370–87. DOI: 10.1039/B915141A.
24. Kochetova N, Animitsa I, Medvedev D, Demin A, Tsiakaras P. Recent activity in the development of proton-conducting oxides for high-temperature applications. RSC Adv. 2016;6(77):73222–68. DOI: 10.1039/C6RA13347A.
25. Lander JJ. The phase system BaO–NiO. J Am Chem Soc. 1951;73(6):2450–2. DOI: 10.1021/ja01150a012.
26. Klinkova LA, Nikolaichik VI, Barkovskii NV, Fedotov VK. New phases in the barium-rich region of the BaO–$BaCuO_2$ system. Bull Russ Acad Sci: Phys. 2009;73(8):1104–6. DOI: 10.3103/S1062873809080243.
27. Zhang W, Osamura K, Ochiai S. Phase diagram of the BaO–CuO binary system. J Am Ceram Soc. 1990;73(7):1958–64. DOI: 10.1111/j.1151–2916.1990.tb05252.x
28. http://www.ihte.uran.ru/?page_id=3142.

Kaimieva O. S., Sabirova I. E., Buyanova E. S., Petrova S. A.
Chimica Techno Acta. 2019. Vol. 6, No. 2. P. 46–50.
ISSN 2409–5613

DOI: 10.15826/chimtech.2019.6.2.02

O. S. Kaimieva[a], I. E. Sabirova[a], E. S. Buyanova[a], S. A. Petrova[b]

[a] *Institute of Natural Sciences and Mathematics, Ural Federal University, 19 Mira st., Ekaterinburg 620002, Russia*
[b] *Institute of Metallurgy, Ural Branch of Academy of Sciences, 101 Amundsena st., Ekaterinburg 620026, Russia*
e-mail: kaimi-olga@mail.ru

Synthesis and Properties of Vanadium Substituted Bismuth Tungstates with Fluorite-like Structure

The samples of vanadium substituted bismuth tungstates with a cubic structure were obtained by solid state method. The unit cell volume of the compounds slightly contracts with increasing tungsten content and in case of vanadium doping. Thermal expansion coefficient of bismuth tungstate is equal to $13 \cdot 10^{-6}$ °C^{-1}. The electrical conductivity was investigated using ac impedance spectroscopy. The results showed that the substitution of tungsten with vanadium ions increased electrical conductivity values by one order of magnitude.

Keywords: bismuth tungstate; fluorite-like structure; oxide-ion conductivity; solid electrolyte.

Received: 05.07.2019. Accepted: 23.07.2019. Published: 05.08.2019.

© Kaimieva O. S., Sabirova I. E., Buyanova E. S., Petrova S. A., 2019

Introduction

δ-Bi_2O_3 has the highest value of electrical conductivity (1–1.5 Ohm^{-1}cm^{-1}) among all known complex oxide electrolyte materials for electrochemical devices [1, 2]. The main disadvantage of this phase is that it is stable only within a limited temperature range (730–825 °C). A large number of studies are connected with searching for the best way of its stabilization at room temperature preserving its characteristics. For this purpose, substitution with various suitable ions (Nb^{5+}, Mo^{6+}, Ta^{5+}, Ti^{4+}, W^{6+} etc.) is usually used [1–4]. It is found for Bi_2O_3-WO_3 system that the introduction of tungsten oxide (more than 9 wt.%) is a necessary condition for stabilization of δ-phase Bi_2O_3 [5]. Otherwise, β-Bi_2O_3 appears. On the other hand, a homogeneity area of cubic structure on the phase diagram exists between compounds with compositions 2:1 and 5:1. Bi_6WO_{12} has fluorite-like structure as well. This compound melts congruently at 1040 °C and has reversible phase transition at 900 °C. So, as it was shown by Wind [6, 7], bismuth tungstates with a fluorite-like structure are promising as compounds which have values of electrical conductivity comparable with those of yttria-stabilized zirconia. Three more stable cubic phases, $Bi_{22}W_5O_{48}$, $Bi_{22}W_{4.5}O_{47.25}$, and $Bi_{23}W_4O_{46.5}$, were obtained at room temperature via quenching [6, 7]. In case of low cooling rate, a phase transition from cubic to tetragonal structure occurs at 700 °C. Until now, many authors have agreed that the phase diagram of Bi_2O_3–WO_3 system is complex enough and requires a de-

tailed study. Takahashi and Iwahara [8] have done research on ionic properties of $(Bi_2O_3)_{1-x}(WO_3)_x$ (x = 0.05–0.5) and found extremely high oxide-ion conductivity for the *fcc* structure over the wide range of temperatures, up to at least 850 °C. The conductivities in $(Bi_2O_3)_{0.78}(WO_3)_{0.22}$ are 0.01 and 0.15 $Ohm^{-1}cm^{-1}$ at 500 and 880 °C, respectively. The oxide ion transfer number is close to 1 down to oxygen partial pressure $p(O_2) = 10^{-15}$ atm [8].

There data on substituted bismuth tungstates $Bi_{22}W_5O_{48}$, $Bi_{22}W_{4.5}O_{47.25}$, $Bi_{23}W_4O_{46.5}$ have not been found in literature. Therefore, the aim of this work is to obtain and study of the structure and physicochemical properties of bismuth tungstates doped with vanadium ions.

Experimental

Samples $Bi_{22}W_{5-x}V_xO_{48-\delta}$, $Bi_{22}W_{4.5-x}V_xO_{47.25-\delta}$, $Bi_{23}W_{4-x}V_xO_{46.5-\delta}$ (x = 0.0; 0.1) were prepared by solid-state method. Metal oxides Bi_2O_3 (99.99 %), WO_3 (99.9 %), V_2O_5 (99.9 %) were taken as precursors. The multi-step synthesis was carried out in the temperature range 400–1000 °C. Annealing time was 8 hour at each stage. The synthesis into pressed bars was performed after annealing of powder samples at 700 °C. The samples were quenched after the last stage of the synthesis. The phase composition of the powders was determined by means of X-ray powder diffraction (DRON3 diffractometer, Russia, Cu Kα radiation). The phase purities of the compounds were confirmed by comparing their XRD patterns with those in the PDF2 database. The density of sintered bars was estimated by Archimedes method.

Dilatometric measurements were carried out on rectangular bars with the length of 23 mm using a DIL 402 C Netzsch dilatometer in the temperature range 20–900 °C with a heating rate of 2 °C/min. The electrical conductivity values were found by ac impedance spectroscopy method (impedance meter Z-3000 "Elins", Russia) using two-probe cell. The measurements were performed in the temperature range 850–200 °C and frequency span 3 MHz — 1 Hz at the cooling mode. Obtained impedance spectra were treated with "ZView" software and equivalent circuits were fitted to them. Using these data, the temperature dependences of electrical conductivity (σ) were plotted in Arrhenius coordinates –lgσ — 1000/T.

Results and discussion

According to results of X-ray diffraction analysis, all obtained compounds were single-phase with cubic structure (space group *Fm*3*m*). X-ray diffraction patterns of the $Bi_{22}W_{5-x}V_xO_{48-\delta}$, $Bi_{22}W_{4.5-x}V_xO_{47.25-\delta}$, $Bi_{23}W_{4-x}V_xO_{46.5-\delta}$ (x = 0.0–0.1) are given in Fig. 1. The unit cell parameters are listed in Table 1. As the radius of vanadium ions is smaller than that of tungsten ions ($r(Bi^{3+})$ = 0.60 Å; $r(W^{6+})$ = 0.60 Å; $r(V^{5+})$ = 0.54 Å [9]), one can observe slight contraction of unit cell volume of the substituted compounds. The same tendency is found for the samples with increasing tungsten content and is reported in [6, 7]. On the whole, all experimental data which are obtained in the present work for matrix compounds are in a good agreement with previous results [6, 7].

For the further dilatometric and electrical conductivity measurements, the bismuth tungstates were pressed and sintered

into bars. Volume porosity of the ceramics obtained at 850 °C was estimated by Archimedes method. The average value was 10 %. For the $Bi_{23}W_4O_{46.5}$ sample, a peak was observed on the cooling curve of thermal expansion coefficient (TEC) near 430 °C (Fig. 2). This peak can be related to the presence of the phase transition from cubic to tetragonal structure [6, 7]. TEC value of the $Bi_{23}W_4O_{46.5}$ equals to $13 \cdot 10^{-6}$ °C^{-1} and is close to that for lanthanum manganite cathode materials. As the temperature of the measurement (900 °C) was higher than that for sintering of the bar (850 °C), there is hysteresis between the heating and cooling curves on the temperature dependence of linear thermal expansion (Fig. 2).

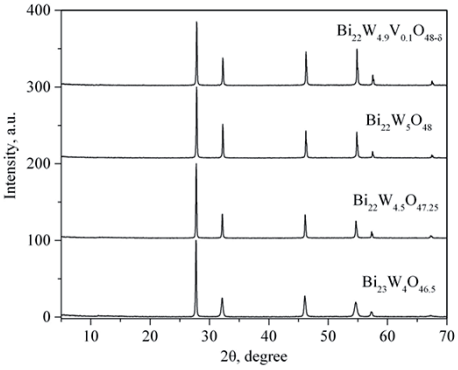

Fig. 1. X-ray diffraction pattern of the bismuth tungstates

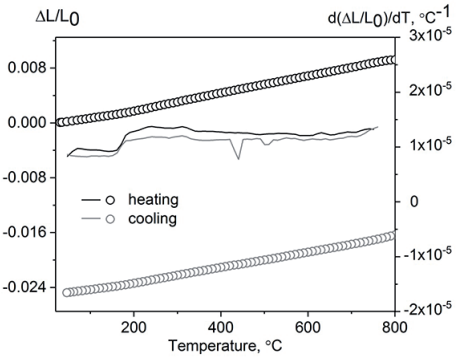

Fig. 2. Temperature dependence of linear thermal expansion and TEC for the sample $Bi_{23}W_4O_{46.5}$

The electrical conductivity was investigated by ac impedance spectroscopy using two-probe method. Introducing of vanadium ions into the structure of bismuth tungstate leads to significant reduction of samples' resistance. The equivalent circuits were matched to impedance spectra to describe processes taking place in the samples during the measurements (Fig. 3). The circuits can be divided into two types. For the high-temperature range, general resistivity of the samples can be defined (R1) (Fig. 3). Other elements of this circuit (R2+CPE1, R3+CPE2) are related to electrode processes because the value of their capacity is equal to 4×10^{-4} F. But at low temperatures it is possible to estimate volume and grain boundary contribution to the electrical conductivity value (Fig. 3). For example, for the composition $Bi_{22}W_{4.9}V_{0.1}O_{48-\delta}$, the volume resistance (R1) equals to 14 kOhm at capacity (CPE1)

Table 1

The unit cell parameters of the bismuth tungstates

Composition	$A \pm 0.001$, Å	$V \pm 0.03$, Å^3
$Bi_{23}W_4O_{46.5}$	5.569	172.73
$Bi_{23}W_{3.9}V_{0.1}O_{46.5-\delta}$	5.569	172.60
$Bi_{22}W_{4.5}O_{47.25}$	5.562	172.05
$Bi_{22}W_{4.4}V_{0.1}O_{47.25-\delta}$	5.558	171.72
$Bi_{22}W_5O_{48}$	5.549	170.85
$Bi_{22}W_{4.9}V_{0.1}O_{48-\delta}$	5.546	170.60

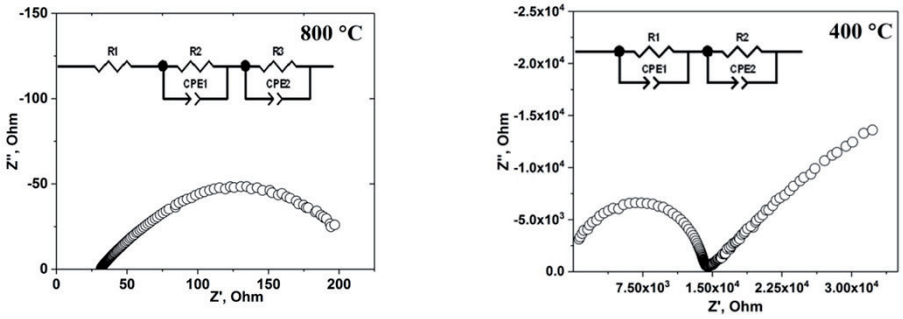

Fig. 3. Impedance spectra of the $Bi_{22}W_{4.9}V_{0.1}O_{48-\delta}$ at 800 °C and 400 °C

3×10^{-11} F, the grain boundary resistance (R2) to 185 kOhm at 2×10^{-5} F (CPE2). Temperature dependences of the general electrical conductivity of the bismuth tungstates were plotted using the data of the impedance spectra (Fig. 4). The results show that the substitution of tungsten with vanadium ions increases electrical conductivity values by one order of magnitude. The activation energy values for all bismuth tungstates are between 0.88–1.02 eV (Table 2), indicating that the samples have ionic type of conductivity. According to our measurements, $Bi_{23}W_{3.9}V_{0.1}O_{46.5-\delta}$ possesses the highest conductivity of all oxides studied (σ_{850} = 0.13 $Ohm^{-1}cm^{-1}$).

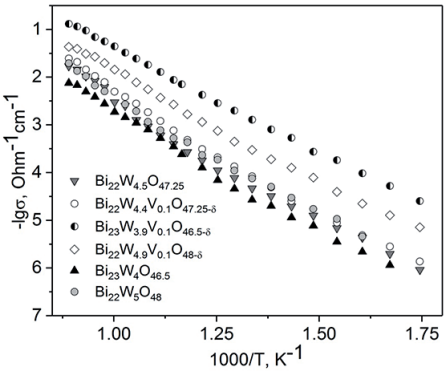

Fig. 4. Temperature dependences of the general electrical conductivity of the bismuth tungstates

Conclusions

To sum up, the solid solutions based on bismuth tungstates with fluorite-like structure were obtained by solid state method. The unit cell volume of the compounds slightly contracts with increasing tungsten content and in case of vanadium doping.

Table 2

Electrical conductivity (σ) and activation energy (E_a) values of the bismuth tungstates

Composition	E_a, eV	σ_{750}, $Ohm^{-1}cm^{-1}$	σ_{500}, $Ohm^{-1}cm^{-1}$
$Bi_{23}W_4O_{46.5}$	0.99	$7.74\cdot10^{-2}$	$1.30\cdot10^{-2}$
$Bi_{23}W_{3.9}V_{0.1}O_{46.5-\delta}$	0.88	$2.85\cdot10^{-1}$	$6.69\cdot10^{-2}$
$Bi_{22}W_{4.5}O_{47.25}$	1.00	$5.92\cdot10^{-3}$	$7.66\cdot10^{-5}$
$Bi_{22}W_{4.4}V_{0.1}O_{47.25-\delta}$	1.02	$7.84\cdot10^{-3}$	$1.30\cdot10^{-4}$
$Bi_{22}W_5O_{48}$	0.92	$1.01\cdot10^{-1}$	$1.91\cdot10^{-2}$
$Bi_{22}W_{4.9}V_{0.1}O_{48-\delta}$	0.95	$1.82\cdot10^{-1}$	$3.50\cdot10^{-2}$

TEC of the $Bi_{23}W_4O_{46.5}$ sample is equal to $13 \cdot 10^{-6}$ °C^{-1}. A small peak on the cooling curve was observed at 430 °C, which can be contributed to the phase transition from cubic to tetragonal phase. The introduction of vanadium ions into bismuth tungstate structure has a positive effect on the electrical conductivity (the $Bi_{23}W_{4.9}V_{0.1}O_{46.5-\delta}$ has the highest value $\sigma_{850} = 0.13$ Ohm^{-1}cm^{-1}).

Acknowledgements

This work was performed within the State Assignment of the Ministry of Education and Science of the Russian Federation no. 4.2288.2017/4.6. Powder X-ray diffraction studies were performed on the equipment of the Ural-M Shared Facility Center of the Institute of Metallurgy of the Ural Branch of the Russian Academy of Sciences (IMET UB RAS).

References

1. Shuk P, Wiemhöfer H-D, Guth U, Göpel W, Greenblatt M. Oxide ion conducting solid electrolytes based on Bi_2O_3. Solid State Ionics. 1996;89:179–96. DOI: 10.1016/0167–2738(96)00348–7.
2. Azad AM, Larose S, Akbar SA. Bismuth oxide-based solid electrolytes for fuel cells. Journal of Materials Science. 1994;29:4135–51. DOI: 10.1007/BF00414192.
3. Ling CD, Johnson M. Modelling, refinement and analysis of the 'Type III' δ-Bi_2O_3-related superstructure in the Bi_2O_3–Nb_2O_5 system. Journal of Solid State Chemistry. 2004;177:1838–46. DOI: 10.1016/j.jssc.2004.01.003.
4. Firman K, Tan KB, Khaw CC, Zainal Z, Tan YP, Chen SK. Doping mechanisms and electrical properties of bismuth tantalite fluorites. Journal of Materials Science. 2017;52:10106–18. DOI: 10.1007/s10853–017–1216–1.
5. Mokhosoev MV, Alekseev FP, Lutsyk VI. Diagrammy sostoyaniya molibdatnykh I vol'framatnykh system [State diagrams of molybdate and tungstate systems]. Novosibirsk: Nauka, 1978. 320 p. Russian.
6. Wind J, Auckett JE, Withers RL, Piltz RO, Maljuk A, Ling CD. Type II $Bi_{1-x}W_xO_{1.5+1.5x}$: a (3+3)-dimensional commensurate modulation that stabilizes the fast-ion conducting delta phase of bismuth oxide. Acta Crystallographica B. 2015;71:679–87. DOI: 10.1107/S2052520615018351.
7. Wind J, Kayser P, Zhang Z, Evans IR, Lind CD. Stability and range of the type II $Bi_{1-x}W_xO_{1.5+1.5x}$ solid solution. Solid State Ionics. 2017;308:173–80. DOI: 10.1016/j.ssi.2017.07.015.
8. Takahashi T, Iwahara H. High oxide ion conduction in sintered oxides of system bismuth oxide — tungsten oxide. Journal of Applied Electrochemistry. 1973;3:65–72. DOI: 10.1007/BF01119469.
9. Shannon RD. Revised Effective Ionic Radii and Systematic Studies of Interatomie Distances in Halides and Chalcogenides. Acta Crystallographica A. 1976;32:751–67. DOI: 10.1107/S0567739476001551.

Kiselev E. A., Gaczynski P., Eckold G.,
Feldhoff A., Becker K.-D., Cherepanov V. A.
Chimica Techno Acta. 2019. Vol. 6, No. 2. P. 51–71.
ISSN 2409–5613

DOI: 10.15826/chimtech.2019.6.2.03

E. A. Kiselev[a], P. Gaczynski[b], G. Eckold[c], A. Feldhoff[d], K.-D. Becker[b], V. A. Cherepanov[a]

[a] *Department of Physical and Inorganic Chemistry, Institute of Natural Sciences and Mathematics, Ural Federal University, Kuybysheva St. 48, 620026, Yekaterinburg, Russia*
[b] *Institute of Physical and Theoretical Chemistry, Technische Universität Braunschweig, Rebenring 56. 10, D-38106, Braunschweig, Germany*
[c] *Institute of Physical Chemistry, Georg-August-Universität Göttingen, Tammannstr. 6, 37077, Göttingen, Germany*
[d] *Institute of Physical Chemistry and Electrochemistry, Leibniz Universität Hannover, Callinstr. 3a, D-30179, Hannover, Germany*
eugene.kiselyov@urfu.ru

Investigations into the structure of $La_3Ni_{2-x}Fe_xO_{7\pm\delta}$

The room-temperature (RT) ^{57}Fe Mössbauer spectra of the $La_3Ni_{2-x}Fe_xO_{7\pm\delta}$ oxide solid solutions of Ruddlesden-Popper-type (x = 0.05, 0.10) reveal two doublets for Fe^{3+} ions in octahedral coordination by oxygen. The existence of two inequivalent sites for Fe at RT is at variance with the space groups *Fmmm* and *Cmcm* (*Amam*) which have been reported for $La_3Ni_2O_{7\pm\delta}$. This unexpected finding is discussed in connection with Patterson analyses and Rietveld refinements of powder XRD data for x = 0, 0.05, and 0.10. Alternative structural models have been proposed which can explain the spectroscopic findings and which are compatible with the results from X-ray diffraction.

Keywords: $La_3Ni_2O_7$; complex oxides; Ruddlesden-Popper phases; Mössbauer spectroscopy; crystal structure; Patterson analysis; Rietveld refinement.

Received: 15.07.2019. Accepted: 01.08.2019. Published: 05.08.2019.

© Kiselev E. A., Gaczynski P., Eckold G., Feldhoff A., Becker K.-D., Cherepanov V. A., 2019

Introduction

Layered Ruddlesden-Popper (R-P) lanthanum nickelates of the general formula $La_{n+1}Ni_nO_{3n+1}$ have recently been studied for potential application as SOFC cathodes [1–5] for the members with n = 1, 2, 3. The structure is characterized by n perovskite-type layers, n·$LaNiO_3$, stacked up in c-direction and separated by a single rock-salt-type layer of LaO, $LaO(LaNiO_3)_n$. Presently, however, $La_2NiO_{4+\delta}$ with n = 1 is the most studied within the series; data concerning $La_3Ni_2O_{7\pm\delta}$ and $La_4Ni_3O_{10-\delta}$ are still insufficient and sometimes contradictory. In the present paper, the focus will be on $La_3Ni_2O_{7\pm\delta}$ (n = 2).

$La_3Ni_2O_{7\pm\delta}$ was first reported by Brisi et al. [6] as an intermediate phase in an attempt to synthesize $La_4Ni_3O_{10-\delta}$ at 1100 °C. Drennan et al. [7] could directly obtain the n = 2 compound by annealing at 1150 °C in air for 5 h with intermediate re-grindings. The unit-cell parameters were approximately determined as a = 5.42 Å, b = 5.47 Å, and c = 20.58 Å. However, electron microscopy revealed intergrowth of all members of the series with n = 2, 3, and 4. Later, the existence of $La_3Ni_2O_{7\pm\delta}$ was confirmed by Odier et al. [8] in the temperature range 900–1150 °C. However, small amounts of secondary phases were

still found present. Mohan Ram et al. [9] obtained $La_3Ni_2O_{7\pm\delta}$ by decomposing stoichiometric amounts of lanthanum and nickel nitrates and annealing at 1420 K for 10 h with frequent grindings. Although the X-ray diffraction patterns showed no evidence for the presence of other members of the series, HREM studies showed intergrowth of small extent of members with $n = 3$ and $n = 5$. Similar problems were also reported by Sreedhar et al. [10] who stated that intergrowth can be minimized by annealing samples at a suitable temperature (1150 °C). According to Zhang et al. [11], single phase $La_3Ni_2O_{7\pm\delta}$ can be obtained by solution synthesis followed by heat treatment and final annealing of the pressed pellets for 4–5 days at 1150–1200 °C. These authors determined the oxygen content of the as-prepared $n = 2$ lanthanum nickelate by iodometric titration and TGA to $La_3Ni_2O_{6.92}$ [11].

Zhang et al. [11] were the first to refine (X-ray) diffraction data of $La_3Ni_2O_{6.92}$ in the orthorhombic space group *Fmmm* which provides only a single site for nickel cations. This space group was also used by Carvalho et al. [12] in their refinement of the unit-cell parameters of the compound. These authors also showed that the oxygen content of as prepared samples depends on the synthesis route: nitrate precursors usually were found to yield oxygen-deficient materials, e. g. $La_3Ni_2O_{6.93}$ which is close to results reported in Ref. [11]. On the other hand, slightly oxygen excess samples, e. g. $La_3Ni_2O_{7.03}$, could be produced by the citrate technique. Generally, least-square refinements of XRD data within the *Fmmm* space group showed good agreement in the unit cell parameters [1, 11–13]. However, neutron diffraction data by Ling et al. [14] on $La_3Ni_2O_{7.02}$ and $La_3Ni_2O_{7.05}$ revealed a number of weak but clearly resolved peaks which could not be indexed by the *Fmmm* structural model, but could satisfactorily be refined within the *Amam* space group (a nonstandard setting of the *Cmcm* space group). The main features of this structure, which also provides a single unique site for nickel, are significantly distorted NiO_6 octahedra and an elongation of Ni–O bonds in *c*-direction towards to the rock salt layers [14]. These results were confirmed by Voronin et al. [15] using single-phase $La_3Ni_2O_{7\pm\delta}$. In this work, the standard *Cmcm* space group was used for refinement of neutron diffraction data and for EXAFS spectral analysis. The unit cell parameters and the oxygen content of the $La_3Ni_2O_{7\pm\delta}$ powder samples obtained by various authors [1, 6, 7, 9–17] are listed in Table 1 for comparison. The temperature dependence of the oxygen content of the $n = 2$ R-P compound in air has been studied by Bannikov and Cherepanov [16] in the temperature range 900–1150 °C. It was shown that the stoichiometric parameter δ of $La_3Ni_2O_{7-\delta}$ changes from about 0.057 at 900 °C to 0.072 at 1150 °C which is in good agreement with the results presented in Refs. [1, 11, 12] for the samples prepared by nitrate route, Table 1.

At elevated temperatures, $La_3Ni_2O_{7\pm\delta}$ has been found to undergo a structural phase transition. Sasaki et al. [13] observed a discontinuous change in the temperature dependence of the lattice parameter for the *c*-axis of the unit cell at about 550 K. The transition has also been detected in lattice expansion [1], in magnetic [18], infrared [19], electrical conductivity [1, 18, 19], and in thermal measurements [18, 20]. From all these experiments, transition temperatures between 550 and 600 K have been reported. More recently, Amow et al. [1] monitored changes in the high-temperature X-ray diffraction patterns

of $La_3Ni_2O_{6.95}$ which led them to the conclusion that at about 590 K a transformation occurs from orthorhombic *Fmmm* to a higher symmetry tetragonal phase.

Mössbauer spectroscopy has already been applied to the neighboring Ruddlesden-Popper phases $La_2Ni_xFe_{1-x}O_{4+\delta}$ (n = 1) [21–24] and $La_4Ni_{3-x}O_{10-\delta}$ (n = 3) [24–26] in a number of studies. The ^{57}Fe Mössbauer spectra of these compounds are composed of one and of two doublets, respectively. This observation is in full agreement with the layered structures of these compounds which provide one unique site and two non-equivalent sites for nickel in the R-P phases with n = 1 and n = 3, respectively. This has been considered strong evidence for the conjecture that Fe is incorporated on the transition metal sites in the R-P lanthanum nickelates. Under this condition — and provided that $La_3Ni_{2-x}Fe_xO_{7\pm\delta}$ crystallizes in space group *Fmmm* or *Cmcm* (*Amam*) — the Mössbauer spectrum of $La_3Ni_{2-x}Fe_xO_{7\pm\delta}$ is expected to consist of a single signal only.

Among the layered Ruddlesden-Popper lanthanum nickelates, $La_3Ni_2O_{7\pm\delta}$ is special in that the average oxidation state of nickel cations for the stoichiometric composition with $\delta = 0$ is 2.5, indicating equal number of Ni^{2+} and Ni^{3+} ions. At low temperatures, this can open the possibility for charge ordering of the nickel cations. Nevertheless, all structural models existing to date for $La_3Ni_2O_{7\pm\delta}$ (*Fmmm* [1, 11–13], *Amam* [14], and *Cmcm* [15]) do not account for this special aspect in providing only a single site for Ni. The present Mössbauer study was undertaken in order to shed light into the local structure of $La_3Ni_{2-x}Fe_xO_{7\pm\delta}$. In contrast to the neighboring R-P phases $La_2Ni_{1-x}Fe_xO_{4+\delta}$ and $La_4Ni_{3-x}Fe_xO_{10-\delta}$ which have already been well studied by Mössbauer spectroscopy [21–26], the present work to our knowledge appears to be the first Mössbauer study of $La_3Ni_{2-x}Fe_xO_{7\pm\delta}$.

Table 1

Structural data of $La_3Ni_2O_{7\pm\delta}$ obtained from X-ray and neutron diffraction, RT

a (Å)	*b* (Å)	*c* (Å)	Space group	Oxygen content 7±δ	Ref.
5.404(2)	5.452(2)	20.442(7)	*Fmmm*	6.95	[1]
5.407(4)	5.454(4)	20.54(2)	—	—	[6]
5.402(2)	5.453(7)	20.537(1)	—	—	[7]
5.412	5.456	20.94	—	—	[9]
5.41	5.46	20.54	—	—	[10]
5.3961(6)	5.4498(5)	20.522(2)	*Fmmm*	6.92	[11]
5.393(2)	5.451(2)	20.54(1)	*Fmmm*	6.93	[12] nitrate route
5.400(2)	5.452(2)	20.52(1)	*Fmmm*	7.03	[12] citrate route
5.3922(1)	5.4488(1)	20.5288(6)	*Fmmm*	6.92	[13]
5.3928(1)*	5.4486(1)*	20.5185(5)*	*Amam**	7.02	[14]
5.3971(2)*	5.4501(2)*	20.507(1)*	*Amam**	7.05	[15]
20.502(1)*	5.4494(7)*	5.3981(7)*	*Cmcm**	—	[16]
5.409(2)	5.452(2)	20.537(3)	—	6.72	[17]

* neutron diffraction at 300 K. Space groups *Amam* and *Cmcm* differ only by the setting of the crystallographic axes.

Experimental

In order to prepare the $La_3Ni_{2-x}Fe_xO_{7\pm\delta}$ (x = 0, 0.05, 0.10) powder samples for our study, stoichiometric amounts of $La(NO_3)_3 \cdot 6H_2O$ (chemical pure grade), $Ni(CH_3COO)_2 \cdot 4H_2O$ (chemical pure grade), and of metallic iron were dissolved in an aqueous solution of nitric acid prepared from concentrated nitric acid (extra pure grade) and deionized water in the ratio 1:3 while heating and mixing on a hot plate. Metallic iron enriched in ^{57}Fe was obtained by reduction of Fe_2O_3 (with iron enriched by 96.6 % in the isotope ^{57}Fe) in flowing H_2 at 925 K for 6 hours and then quantitatively transferred into solution. Subsequently, citric acid monohydrate $C_6H_5O_4(OH)_3 \cdot H_2O$ (chemical pure grade) was added to the solution as a chelating and gelling agent. The thus-prepared precursor solution was dried and decomposed forming a brown powder. The powder was calcined in air at 1273 K for 30 minutes to remove organic and carbon residuals and then cooled down to RT. The dark grey product was ground, pressed into pellets and annealed in air at 1373 K for 24 h. In order to obtain single-phase $La_3Ni_{2-x}Fe_xO_{7\pm\delta}$ materials (x = 0, 0.05, 0.10), 5–6 intermediate cycles of regrinding, pelletizing and annealing at 1373 K were required. Sample purity and morphology was checked by REM/EDX analysis (Jeol JSM-6510, Bruker Nano XFlash 410). The measurements confirmed the absence of any impurities and secondary phases in noticeable concentrations.

Phase composition and crystal structure of the synthesized samples were examined by powder X-ray diffraction using an Equinox 3000 diffractometer (INEL, France) with Cu-Kα radiation (λ = 1.54178 Å); data were collected in the asymmetric reflection mode. The scattered radiation from the flat-plate samples was registered by a curved position-sensitive detector (CPS-590) within the angle interval 10–90° in 2θ. The detector was calibrated using $Na_2Al_2Ca_3F_{14}$ as standard. The data acquisition time was 1 h for phase analysis and 17–21 h for structural analysis.

All calculations including the Rietveld refinements and determinations of crystal structure of samples studied were performed using the FullProf package [27]. The following structural parameters were varied in the refinement procedure: scale factor, unit cell parameters, zero shift, atomic positions, overall displacement parameters (B-factors, B_{ov}), background, peak shape, and width parameters. The peak profiles were described by the Thompson-Cox-Hasting pseudo-Voigt function within the anisotropic strain broadening model. The instrumental resolution function was determined by means of diffraction experiments with a CeO_2 reference sample which had been annealed twice at 1473 K for 48 h with intermediate regrinding and then slowly cooled down to RT. The background was estimated by linear interpolation between manually selected background points with refinable heights.

Transmission ^{57}Fe Mössbauer spectra were taken using a standard Mössbauer system (Halder) in the sinusoidal driving mode employing a $^{57}Co/Rh$ γ-source with a maximum activity of 1.91 GBq. The relatively low iron content and high electronic mass-absorption coefficient of $La_3Ni_{2-x}Fe_xO_{7\pm\delta}$ for the 14.4 keV Mössbauer γ-radiation necessitated the use of samples enriched in ^{57}Fe, see above. The least square fits of the spectra using lorentzian line shapes were performed by means of the *Recoil* Mössbauer data evaluation software [28] yielding the fol-

lowing parameters: isomershift *IS* (mm·s^{-1}) relative to α-Fe at RT, quadrupole splitting *QS* (mm·s^{-1}) of doublets, full width *Γ* (mm·s^{-1}) at half maximum of lines, and (relative) spectral area *A* (%) of spectra.

Mössbauer spectroscopy

The RT ^{57}Fe Mössbauer spectra of $La_3Ni_{2-x}Fe_xO_{7\pm\delta}$ (x = 0.05, 0.10) are displayed in Fig. 1.

The highly symmetric spectra are composed of two quadrupole-split doublets of almost identical intensity. This observation gives evidence of the fact that iron cations are incorporated on two inequivalent lattice sites which at present will be denoted by A and B for the site with the smaller and the larger quadrupole splitting (*QS*), respectively, $QS(Fe_A) < QS(Fe_B)$. The parameters obtained from the least square fits of the spectra are presented in Table 2.

The isomer shifts (*IS*) of 0.31 mm·s^{-1} of the two subspectra of $La_3Ni_{2-x}Fe_xO_{7\pm\delta}$ are identical in the two solid solutions studied (x = 0.05 and 0.10). It is also to be noted that these values are in close agreement with the ^{57}Fe isomer shifts observed for the other octahedrally coordinated $La_{n+1}Ni_nO_{3n+1}$ R-P phases with n = 1 and n = 3 [21–26]. According to numerous Mössbauer studies, e.g. Refs. [29, 30], such *IS*-values are characteristic for high-spin Fe^{3+} ions octahedrally coordinated by oxygen.

The RT quadrupole splittings (*QS*) of the two doublets in $La_3Ni_{2-x}Fe_xO_{7\pm\delta}$ are found to differ significantly with values of about 0.43 mm·s^{-1} and 0.95 mm·s^{-1} for iron incorporated on sites of type A and B, respectively, Table 2. As also seen, Fig. 1, transmission can assume values as low as about 90 % in parts of the spectra. Therefore, the absorbers used in the present study have to be characterized as "thick". This conclusion is also supported by the RT line widths of the two samples which take values ranging between 0.26 and 0.31 mm·s^{-1} and, thus, reveal significant broadening in comparison with the theoretical width of a ^{57}Fe Mössbauer line of about 0.20 mm·s^{-1} for "thin"

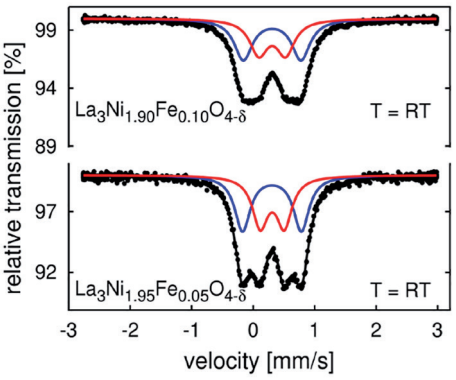

Fig. 1. ^{57}Fe Mössbauer spectra of $La_3Ni_{2-x}Fe_xO_{7\pm\delta}$ (x = 0.05 and 0.10) at RT

Table 2

Parameters of the RT ^{57}Fe Mössbauer spectra of $La_3Ni_{2-x}Fe_xO_{7\pm\delta}$ (x = 0.05 and 0.10): *IS* — isomer shift (vs α-Fe), *QS* — quadrupolar splitting, Γ — full line width at half maximum (FWHM), *A* — experimental area fraction

Compound	*IS* (mm·s^{-1})	*QS* (mm·s^{-1})	Γ (mm·s^{-1})	*A* (%)	site
$La_3Ni_{1.95}Fe_{0.05}O_{7\pm\delta}$	0.31	0.41	0.30	50	A
	0.31	0.97	0.26	50	B
$La_3Ni_{1.90}Fe_{0.10}O_{7\pm\delta}$	0.31	0.46	0.31	47	A
	0.31	0.93	0.28	53	B

absorbers. In addition to line broadening, the thickness effect can also give rise to intensity distortion in the spectra as will be discussed below.

Predominantly, low transmission and broadening of the experimental Mössbauer lines can be attributed to the substitution of nickel by iron strongly enriched in ^{57}Fe (96.6 %) which causes large values for the total absorber thickness t_a of the samples. In the present case with ^{57}Fe on two sites of the structure, t_a it is defined as $t_a = (f_A\ N_A + f_B\ N_B)\cdot\sigma_0$ [31]. Here, f_ε represents the Debye-Waller factor of atoms of type ε (ε = A, B) and N_ε their number per cm^2 of absorber; $\sigma_0 = 2.56\cdot10^{-18}$ cm^2 is the absorption cross section of a Mössbauer atom. In the present work, an estimate of 0.75 can be assumed for the RT Debye-Waller factor. Using this approximate value, estimates of about $t_a = 4.0$ and 8.0 are obtained for total absorber thicknesses of the $La_3Ni_{2-x}Fe_xO_{7\pm\delta}$ samples with $x = 0.05$ and 0.10, respectively, Fig. 1.

For non-overlapping doublets of lorentzian shape, these t_a-values would give rise to theoretical line widths of about 0.23 mm·s^{-1} and 0.25 mm·s^{-1} for $x = 0.05$ and 0.10, respectively, see e. g. Refs. [29, 31]. However, as seen, Fig.1, doublets are overlapping to various degree. Notably the inner doublet A is almost fully overlapped by doublet B. In the limit of full overlap, theoretical line widths amount to about 0.25 mm·s^{-1} and 0.30 mm·s^{-1} for $x = 0.05$ and $x = 0.1$, respectively [29, 31]. Indeed, in agreement with these expectations, line widths observed for the inner doublet, A, are always larger than those of doublet B, Table 2. Remaining discrepancies between theoretical and experimental line widths can easily be attributed to the fact that quadrupolar interactions of the iron nuclei possess a distribution, see below, which provides an additional source for line broadening. As a further consequence of the present large values of total absorber thickness t_a, spectra undergo intensity distortion which always causes an underestimation of large spectral contributions on the basis of experimental signal areas. As has been demonstrated by Rancourt [31], such intensity corrections can be very large. In the present case, however, they are almost nonexistent ($x = 0.05$) or very moderate (~ 2 % for $x = 0.10$) due to the (almost) equal areas of the two experimental doublets. Thus, in the present case corrections to experimental signal intensities can well be neglected.

Crystal structure

As discussed in the Introduction, to date the crystal structure of $La_3Ni_2O_{7\pm\delta}$ has been assigned to the orthorhombic space groups *Fmmm* (№ 69) [1, 11–13] or *Cmcm* (№ 63) [14, 15]. According to these structural models, lanthanum cations occupy two different crystallographic positions, but the nickel cations are located on a single site exclusively. This is in striking contrast with the present results of the Mössbauer measurements which clearly indicate the existence of two nonequivalent lattice sites for iron/nickel in the studied $La_3Ni_{2-x}Fe_xO_{7\pm\delta}$ solid solutions at RT. In order to explain the unexpected observations made in Mössbauer spectroscopy for the $n = 2$ member of the R-P series, in the following an attempt will be undertaken to search for adequate structural models of $La_3Ni_{2-x}Fe_xO_{7\pm\delta}$ ($x \geq 0$) accounting for two inequivalent Ni/Fe sites.

The XRD patterns of the synthesized $La_3Ni_{2-x}Fe_xO_{7\pm\delta}$ ($x = 0$, 0.05, 0.10) powder samples were indexed in orthorhom-

bic symmetry. Unit cell parameters a = 20.52298 Å, b = 5.45805 Å, c = 5.40101 Å, ($\alpha = \beta = \gamma = 90°$) of $La_3Ni_{1.9}Fe_{0.1}O_{7\pm\delta}$ were obtained with the help of the DICVOL04 program [32] and the figures of merit provided by this analysis amounted to M(20) = 56.2, F(20) = 60.7. Calculations by means of the ITO program [33] resulted in a preferable face-centered space group with almost the same unit cell parameters of a = 5.4577Å, b = 20.5225Å, and c = 5.4020 ($\alpha = \beta = \gamma = 90°$), and a figure of merit F(20) = 59.3. After preliminary profile-matching refinement within primitive orthorhombic *Pmmm*, probable space groups were searched for by means of the CheckGroup program interfaced by WinPlotr [34]. Thus, 48 possible space groups were obtained for consideration. Most of them are primitive with quite low values for figures of merit (<1.35). In order to reduce the number of space groups, we focused on those which can be deduced from group-subgroup relations keeping both unit cell dimensions and orthorhombic crystal system of the parent group unchanged. Referring to International Tables for Crystallography [35] only 6 subgroups remained: *Ccca* (No 68), *Cmma* (No 67), *Cccm* (No 66), *Cmmm* (No 65), *Cmca* (No 64), and *Cmcm* (No 63). Bearing in mind the results of Mössbauer spectroscopy that reveal the existence of two nonequivalent sites for iron/nickel ions, the list of possible space groups shortens to three: *Cmmm* (No 65), *Cmma* (No 67), and *Bmmb* (non-standard setting of *Cmcm* space group*)* (No 63).

The next step of our study was an attempt to determine the crystal structure of $La_3Ni_{1.9}Fe_{0.1}O_{7\pm\delta}$ from XRD patterns by constructing the Patterson maps using observed structure amplitudes and the peak search procedure of the GFourier program [34]. The Patterson maps were constructed from the structural amplitudes extracted during the profile-matching fit according to the Le Bail algorithm for each chosen space group.

Note that the simplest crystal structure solutions should be expected for both *Fmmm* and *Cmmm* models because these space groups correspond to exactly the same Patterson space groups *Fmmm* and *Cmmm* [35]. This means that one has exactly the same symmetry both in real space and Patterson space. As far as for X-ray diffraction, both nickel and iron atoms are indistinguishable and, thus, $La_3Ni_{1.9}Fe_{0.1}O_{7\pm\delta}$ contains three types of atoms with substantially different numbers of electrons. Consequently, the observed peaks on the Patterson map might be resolved except for those having the same interatomic distances, for example the La1-La1 and Ni-Ni bond lengths in the perovskite layers of the *Fmmm* structure. Additionally, if the heaviest atom (La) is placed into the origin of the unit cell with coordinates (0, 0, 0) — as we did in the present case — then the peaks observed in Patterson space relate to interatomic vectors with coordinates ($u = \pm\{x\text{-}0\}$, $v = \pm\{y\text{-}0\}$, $w = \pm\{z\text{-}0\}$) and coincide with atomic positions ($\pm x$, $\pm y$, $\pm z$) in real space. Accounting for these considerations, we were able to solve the crystal structure for $La_3Ni_{1.9}Fe_{0.1}O_{7\pm\delta}$ in the framework of *Fmmm* and *Cmmm* space groups directly from the peaks observed in Patterson maps. The results of the crystal structure solutions for $La_3Ni_{1.9}Fe_{0.1}O_{7\pm\delta}$, which are summarized in Table 3, confirm our above mentioned expectations.

As can be seen from Table 3, only a single crystallographic position is available for nickel/iron cations within the *Fmmm* crystal structure of $La_3Ni_{1.9}Fe_{0.1}O_{7\pm\delta}$. This is in agreement with the earlier pro-

Table 3

Crystal structure solutions for $La_3Ni_{1.9}Fe_{0.1}O_{7\pm\delta}$ according to *Fmmm* and *Cmmm* models obtained from Patterson maps using peak search procedure of GFourier program [34]

Peak No	Relative atomic coordinates			Occupation	Peak height	Wyckoff position	Type of atom
	X	*Y*	*Z*				
Fmmm (69): *a* = 5.4020Å, *b* = 5.4570Å, *c* = 20.5170 Å *general multiplicity 32*							
1	0	0	0	0.125	9872	4*a*	La1
2	0	0	0.1837	0.25	6488	8*i*	La2
3	0	0	0.4067	0.25	4024	8*i*	Ni
4	0	0	0.5	0.125	1293	4*b*	O1
5	0	0	0.3076	0.25	1238	8*i*	O2
6	0.25	0.25	0.0922	0.5	1067	16*j*	O3
Cmmm (65): *a* = 5.4014Å, *b* = 5.4576Å, *c* = 20.5182 Å *general multiplicity 16*							
1	0	0	0	0.125	9892	2*a*	La1
2	0	0.5	0.5	0.125	8427	2*c*	La2
3	0	0.5	0.3158	0.25	6163	4*l*	La4
4	0	0	0.1830	0.25	5778	4*k*	La3
5	0	0.5	0.0907	0.25	3864	4*l*	Ni2
6	0	0	0.4035	0.25	3855	4*k*	Ni1
7	0	0.5	0.1990	0.25	1105	4*l*	O4
8	0.25	0.25	0.0925	0.5	1028	8*m*	O6
9	0.25	0.25	0.4030	0.5	992	8*m*	O5
10	0	0.5	0	0.125	937	2*b*	O1
11	0	0	0.4922*	0.25*	987	4*l**	O2
12	0	0	0.2992	0.125	881	4*k*	O3

* here *Z* should be 0.5, the occupancy equal to 0.125 and the Wyckoff position should be 2*d* according to the chemical composition $La_3Ni_{1.9}Fe_{0.1}O_7$

posed *Fmmm* space group for undoped $La_3Ni_2O_{6.92}$ by Zhang et al. [11]. The main difference is that we place lanthanum into position (4a) at the origin of the unit cell (0, 0, 0). Zhang puts one of the oxygen anions in that position (4a) and the lanthanum cations in position 4b with relative coordinates (0, 0, 0.5). In contrast, the *Cmmm* space group possesses two different crystallographic sites (4k and 4l) for nickel cations. Thus, the *Cmmm* model can provide an explanation for the observed RT Mössbauer spectra of the $La_3Ni_{2-x}Fe_xO_{7\pm\delta}$ solid solutions (x = 0.05, 0.1).

In addition, it is worth noting that the space groups under consideration are subgroups of the space group *Fmmm*. Thus, if the Wyckoff positions of each atom in *Fmmm* are known, we can easily deduce the Wyckoff positions of each atom in the corresponding subgroup. The transformation of atomic coordinates from *Fmmm* (Table 3) to the corresponding subgroups was performed by the Pow-

derCell program [36] in order to reveal the possibility for the appearance of non-equivalent positions for nickel cations. As a result, of the six subgroups considered, only three would meet the latter criterion, namely *Cmma* (№ 67), *Cmmm* (№ 65), and *Bmmb* (№ 63) — a non-standard setting of the *Cmcm* space group.

The Rietveld analysis of XRD patterns for $La_3Ni_{2-x}Fe_xO_{7\pm\delta}$ within the suggested crystal structure models as well as thorough search for additional reflections with even tiny intensities which could definitely be attributed to a particular space group did not allow us to arrive at a final conclusion. As an example, Fig. 2 illustrates the refined Rietveld powder profiles of $La_3Ni_{2-x}Fe_xO_{7\pm\delta}$ solid solutions within space groups *Cmmm* (A), *Cmma* (B), and *Bmmb* (C). Table 4 summarizes *R*-factors and chi-square values (χ^2) for all refined patterns in the framework of the proposed structural models with two inequivalent sites for Ni/Fe — space group *Fmmm* which provides only a single site for Ni/Fe is included for comparison. On the basis of these R-factor and χ^2 data, the following observations can be made: (i) *Fmmm* appears the least probable space group, (ii) fits within *Cmmm* and *Cmma* appear slightly superior to *Bmmb*, (iii) no significant differences can be observed between *Cmmm* and *Cmma*. Therefore, no valid conclusion can be drawn in respect to the true space group of $La_3Ni_{2-x}Fe_xO_{7\pm\delta}$ on the basis of the present X-ray diffraction data.

Table 5 and Table 6 report the results of the Rietveld refinements for $La_3Ni_{2-x}Fe_xO_{7\pm\delta}$ in the two most probable space groups *Cmma* and *Cmmm*, respectively. The crystal structures of $La_3Ni_{2-x}Fe_xO_{7\pm\delta}$ (x = 0, 0.05, 0.10) solid solutions confined to space groups *Cmmm*, *Cmma*, and *Bmmb* with two inequivalent sites (Ni1 and Ni2) for Ni/Fe are shown in Fig. 3. For reason of comparison, the graph also shows the structural model for space group *Fmmm*. As can be seen from Fig. 3, in all cases the lattice is built up from double perovskite layers $2[La(Ni/Fe)O_3]$ which are stacked between single rock-salt LaO layers along the *c*-axis. In *Cmmm*, *Cmma*, and *Bmmb*, the double perovskite layers consist of two different Ni/FeO_6 octahedra (Ni1, Ni2) with slightly different distortions. Within the double perovskite layers the differently distorted octahedral Ni/Fe sites are arranged in different ways, Fig. 3B-D.

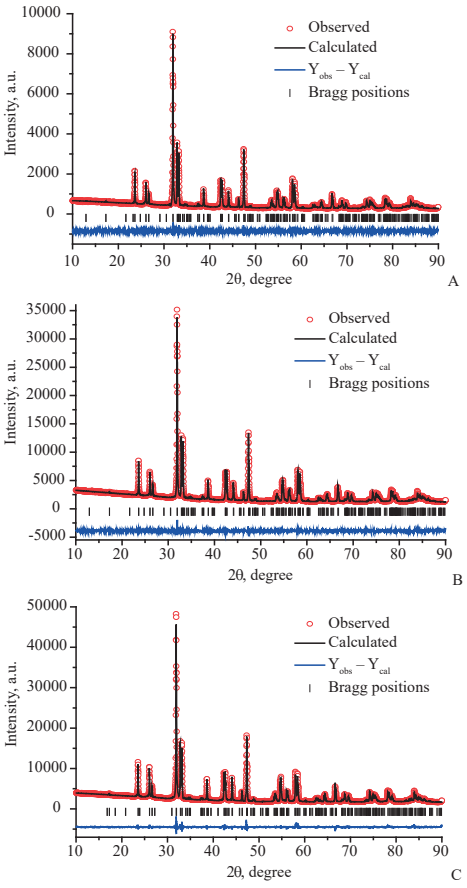

Fig. 2. Rietveld refined XRD powder patterns of $La_3Ni_{2-x}Fe_xO_{7\pm\delta}$ solid solutions within space groups *Cmmm* for x = 0 (A), *Cmma* for x = 0.05 (B), and *Bmmb* for x = 0.10 (C)

Finally, *a*- and *b*-parameters and the unit cell volume *V* of the $La_3Ni_{2-x}Fe_xO_{7\pm\delta}$ solid solutions are found to increase with Fe content (*x*), (see Tables 5 and Table 6) which are in good agreement with size factor for 3*d*-metal cations: $r(Fe^{3+}) = 79$ pm > $r(Ni^{3+})$ = 74 pm [37].

Table 4

Comparison of *R*-factors and χ^2-values obtained for structural models of $La_3Ni_{2-x}Fe_xO_{7\pm\delta}$ solid solutions after Rietveld refinement

Iron content	Space group	R_p	R_{wp}	R_{exp}	χ^2
$x = 0$	*Fmmm*	4.65	6.02	4.56	1.74
	Cmma	4.38	5.71	4.59	1.55
	Cmmm	4.36	5.69	4.58	1.54
	Bmmb	4.51	5.86	4.58	1.64
$x = 0.05$	*Fmmm*	2.85	3.89	2.19	3.16
	Cmma	2.55	3.51	2.17	2.62
	Cmmm	2.56	3.54	2.17	2.68
	Bmmb	2.64	3.66	2.18	2.83
$x = 0.1$	*Fmmm*	2.95	4.17	1.90	4.82
	Cmma	2.84	3.99	1.89	4.46
	Cmmm	2.96	4.15	1.91	4.72
	Bmmb	2.82	4.03	1.89	4.53

Table 5

Rietveld refined atomic coordinates and bond lengths *L*(Ni-O) for $La_3Ni_{2-x}Fe_xO_7$ ($x = 0$, 0.05, 0.10) solid solutions within the *Cmma* model: *4g*: La1 — (0,0.25,0.25), O3 — (0,0.25,0.75), La2,3/Ni1,2/O1,2 — (0,0.25,*Z*); *8l*:O4,5 — (0.25,0,*Z*), RT

Refined parameter	$x = 0$	$x = 0.05$	$x = 0.10$
zero point	0.025(1)	-0.0044(8)	0.0038(8)
B_{ov}, Å^2	1.66(4)	1.50(3)	1.58(3)
a, Å	5.3895(1)	5.3970(1)	5.4019(1)
b, Å	5.4462(1)	5.4521(1)	5.4574(1)
c, Å	20.5250(3)	20.5280(2)	20.5192(2)
V, Å^3	602.46(1)	604.04(1)	604.91(1)
Z(La2)	0.06994	0.06994	0.07007
Z(La3)	0.43006	0.43006	0.42993
Z(Ni1)	0.8476(2)	0.8472(1)	0.8469(1)
Z(Ni2)	0.6524(2)	0.6528(1)	0.6531(1)
Z(O1)	0.9526(6)	0.9454(7)	0.94918
Z(O2)	0.5474(6)	0.54719	0.55082
Z(O4)	0.6448(9)	0.6415(5)	0.6439(6)

Continuation of table 5

Refined parameter	$x = 0$	$x = 0.05$	$x = 0.10$
Z(O5)	0.838(1)	0.8370(7)	0.8389(8)
L(Ni1-O3), Å	2.003(4)	1.995(2)	1.988(3)
L(Ni1/Ni2-O1/O2), Å	2.16(1)	2.01(1)	2.099(3)
4L(Ni1-O5), Å	1.926(2)	1.929(2)	1.927(2)
Average L(Ni1-O), Å	1.977(2)	1.954(3)	1.9657(8)
L(Ni2-O3), Å	2.003(4)	2.169(2)	1.988(3)
4L(Ni2-O4), Å	1.922(2)	1.932(1)	1.929(2)
Average L(Ni2-O), Å	1.974(2)	1.9818(7)	1.967(5)

Table 6

Rietveld refined relative atomic coordinates and bond-lengths L(Ni-O) for $La_3Ni_{2-x}Fe_xO_7$ ($x = 0$, 0.05, 0.10) solid solutions within the *Cmmm* model: *2a*: La1 — (0, 0, 0), *2b*: O1 — (0, 0.5, 0) *2c*: La2 — (0,0.5,0.5), *2d*:O2 – (0, 0, 0.5), *4k*: La3/Ni1/O3 — (0, 0, Z), *4l*: La4/Ni2/O4 — (0, 0.5, Z), *8m*: O5/O6 — (0.25, 0.25, Z), RT

Refined parameter	$x = 0$	$x = 0.05$	$x = 0.10$
zero point	0.025(1)	-0.0043(8)	0.0038(8)
B_{ov}, Å^2	1.66(4)	1.47(3)	1.61(3)
a, Å	5.3895(1)	5.3971(1)	5.4019(1)
b, Å	5.4462(1)	5.4521(1)	5.4574(1)
c, Å	20.5250(3)	20.5279(2)	20.5191(2)
V, Å^3	602.46(1)	604.044(8)	604.91(1)
Z(La3)	0.18006	0.18016	0.17993
Z(La4)	0.31994	0.31984	0.32007
Z(Ni1)	0.4024(2)	0.4029 (1)	0.4031(1)
Z(Ni2)	0.0976(2)	0.0971 (1)	0.0969(1)
Z(O3)	0.298(1)	0.30079	0.2952(9)
Z(O4)	0.20267	0.2049 (8)	0.19918
Z(O5)	0.3943(9)	0.4016 (3)	0.4021(4)
Z(O6)	0.087(1)	0.0984 (3)	0.0979(4)
L(Ni1/Ni2-O2/O1), Å	2.003(4)	1.994(2)	1.989(3)
L(Ni1-O3), Å	2.15(3)	2.095(2)	2.21(2)
4L(Ni1/Ni2-O5/O6), Å	1.923(2)	1.9181(1)	1.9198(1)
Average L(Ni1-O), Å	1.974(4)	1.9603(5)	1.980(3)
L(Ni2-O4), Å	2.157(4)	2.21(2)	2.099(3)
Average L(Ni2-O), Å	1.979(1)	1.980(3)	1.944(4)

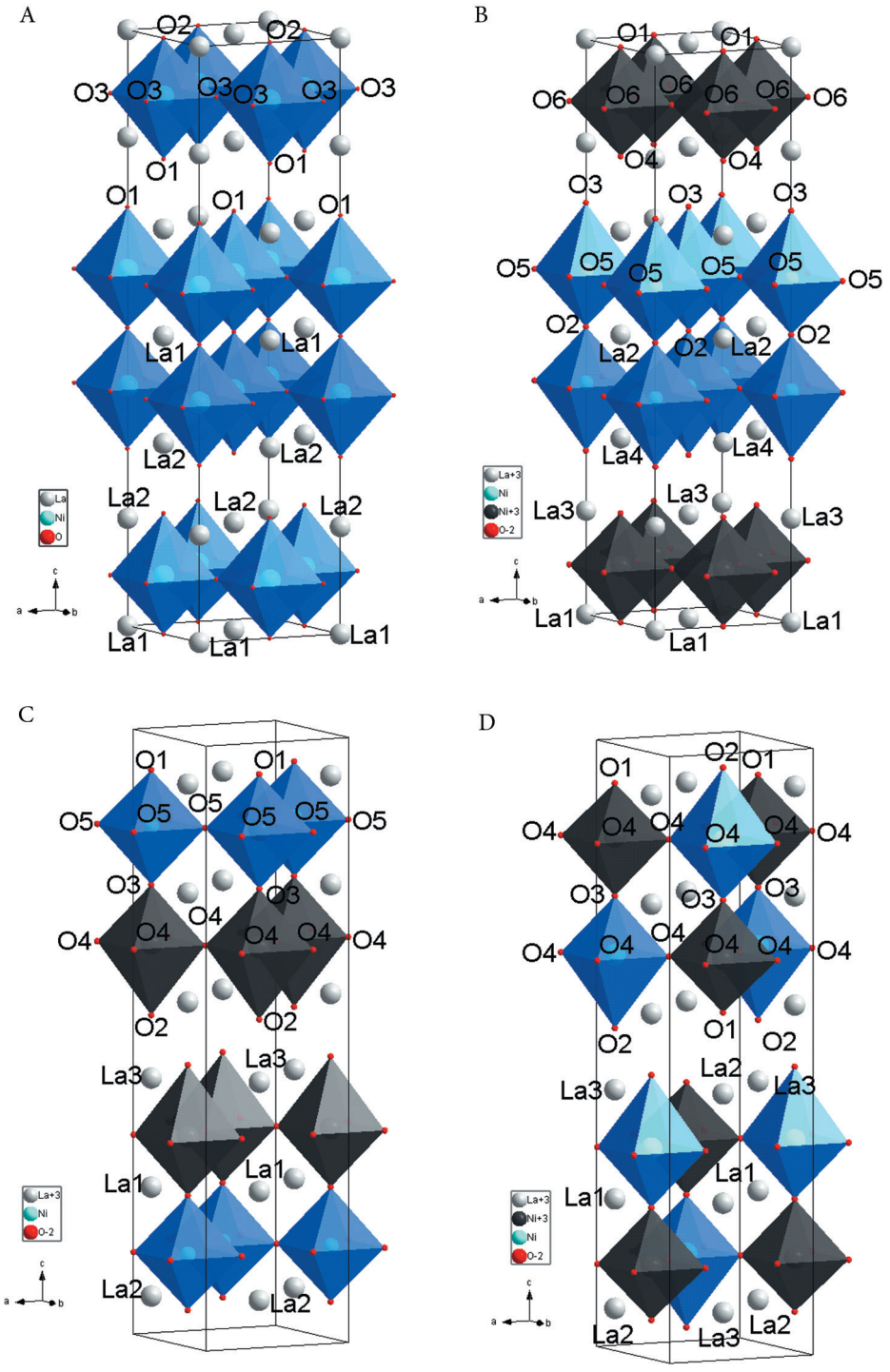

Fig. 3. Crystal structures of $La_3Ni_{2-x}Fe_xO_7$ solid solutions within space groups *Fmmm* (A), *Cmmm* (B), *Cmma* (C), and *Bmmb* (D): grey balls — La^{3+}, blue and dark grey octahedra represent oxygen environments of nickel/iron cations on Ni1- and Ni2-sites, respectively

Discussion

The RT Mössbauer spectra of $La_3Ni_{2-x}Fe_xO_{7\pm\delta}$ reveal that the sites for iron are characterized by two significantly different quadrupolar interactions, Table 2. In general, the ^{57}Fe Mössbauer quadrupole splitting is given by [29]

$$QS = \frac{1}{2} eQV_{zz} \sqrt{1 + \frac{1}{3}\eta^2} \qquad (1)$$

where the so-called asymmetry parameter η is defined as $\eta = (V_{xx} - V_{yy})/V_{zz}$ ($0 \le \eta \le 1$) and where $V_{\alpha\alpha}$ ($\alpha = x, y, z$) represent the electric field gradients (EFGs) at the nucleus in the principal axis system with $|V_{zz}| \ge |V_{yy}| \ge |V_{xx}|$. Q denotes the quadrupole moment of the first excited nuclear state of ^{57}Fe and e is the proton charge. In the case of Fe^{3+} ions possessing the d^5 electronic configuration it is reasonable to assume that the experimental quadrupole splittings are dominated by the so-called lattice contribution to the electric field gradient which is determined by the positions and charges of the ions surrounding the Mössbauer atoms in the lattice. According to Eq. (1), the quadrupole interaction is sensitive to local symmetry around the nuclear probes in that $\eta = 0$ for local tetragonal symmetry and that the interaction vanishes for local cubic symmetry, $V_{zz} = 0$. Thus, the splittings reflect an asymmetry of the charge distribution in the crystal lattice around the nuclear probes and notably also the local distortion of their coordination polyhedra.

The RT Mössbauer data clearly reveal that the two sites, A and B, occupied by iron differ significantly in respect to the quadrupolar interactions experienced by the probe nuclei, $QS(Fe_A) < QS(Fe_B)$, Table 2. Under the assumption that iron substitutes for nickel, this experimental finding is in conflict with the structural assignments made to date for $La_3Ni_2O_{7\pm\delta}$, i. e. space groups *Fmmm* [1, 11–13], *Amam* [14], and *Cmcm* [15], which provide only one unique site for Ni/Fe in the structure. The assumption made here that iron adopts nickel sites is strongly supported by successful predictions made in respect to the neighboring R-P phases $La_2Ni_{1-x}Fe_xO_{4+\delta}$ [21–24] and $La_4Ni_{3-x}Fe_xO_{10-\delta}$ [24,26]. Their ^{57}Fe Mössbauer spectra are composed — as predicted on the basis of their layered R-P structures — of one and of two doublets, respectively. Further on, this assumption is also supported by crystal chemical arguments for the transition metal cations which make high-spin Fe^{3+} ions with their intermediate ionic radius of 79 pm a perfect substitute for both high-spin Ni^{3+} (74 pm) and Ni^{2+} (83 pm) cations [37]. Thus, provided that iron substitutes for nickel and that one of the aforementioned space groups applies, only one signal is expected in the Mössbauer spectrum of $La_3Ni_{2-x}Fe_xO_{7\pm\delta}$ ($x > 0$) which is in contrast with experiment.

Two possible explanations can be offered for this unexpected observation of two nonequivalent sites for Fe/Ni. The first would be the conjecture that the $La_3Ni_{2-x}Fe_xO_{7\pm\delta}$ solid solutions at RT adopt a lower symmetry than hitherto assumed. This approach has been followed in Crystal structure section, where possible structural models have been indicated. The second explanation, which will be discussed below, involves a local reconstruction of the R-P layer structure.

Indeed, a low-symmetry phase at RT cannot be unexpected in view of the fact that the mixed-valent $La_3Ni_{2-x}Fe_xO_{7\pm\delta}$ contains Ni^{3+} and Ni^{2+} cations in similar concentrations

$$[Ni^{2+}] = 1 \mp 2\delta$$

and

$$[Ni^{3+}] = 1 \pm 2\delta - x \qquad (2)$$

where square brackets denote the number of species per formula unit. The validity of Eq. (2) is based on the assumption that iron is always in the trivalent charge state as revealed by the present Mössbauer spectra (see Mössbauer spectroscopy section) and discussion below. The close agreement of $[Ni^{2+}]$ and $[Ni^{3+}]$ could give rise to charge ordering and to the formation of some kind of lower symmetry structure. Indeed, charge ordering in $La_3Ni_2O_{7-\delta}$ at low temperatures has already been discussed by Taniguchi et al. [38] where it was proposed that ordering of electronic charge on nickel was induced by ordering of oxygen vacancies. In the same context, electrical conductivity, which is intimately related with electronic materials properties, has given clear evidence of a transition from temperature-activated behavior to metal-type conduction at high temperatures with reported transition temperatures of 550 K [1, 18] and 600 K [19].

As evidenced by the RT Mössbauer spectra, Fe^{3+} cations are almost evenly distributed between the two nonequivalent Ni1- and Ni2-sites for Ni/Fe in the lattice, Table 2. This can easily be explained as follows. During their synthesis, samples have been exposed to high temperatures (up to 1373 K) where according to the above discussion there is only one unique site for Ni/Fe and the Fe dopant will be randomly distributed on this unique site. Electronic charge ordering on the nickel cations leading to less symmetric structure occurs at much lower temperatures where Fe^{3+} cations are not mobile anymore and, due to their random distribution on available sites, show up in almost equal proportions on the Ni1- and Ni2-sites which occur in equal numbers in the alternative structures previously discussed, Tables 4–6 and Fig. 3. Due to their fixed valence (see Mössbauer spectroscopy section) and discussion below, Fe^{3+} cations are not part of the electronic ordering process and, thus, serve as "spectators" of the structural changes induced by the evolving electronic charge order-disorder.

In an ideally stoichiometric system, where $x = 0$ and $\delta = 0$, Ni^{2+} and Ni^{3+} ions are present in exactly equal numbers, Eq. (2), and distributed over the two nonequivalent sites, Ni1 and Ni2, of the structure. Thus, two limiting cases of the cation distribution are to be considered. In one case — cation distribution (I) — all sites of Ni1-type are occupied by (all) Ni^{2+} ions and, correspondingly, all Ni2-sites are occupied by (all) Ni^{3+} ions. In the case of cation distribution (II), all Ni1-sites are occupied by Ni^{3+} and all Ni2-sites by Ni^{2+}. In both situations, different, but single-valued electric field gradients (EFG) are expected at the two inequivalent sites of the structure due to the fully ordered distribution of charges in the lattice. However, already the introduction of Fe^{3+} ions into sites of the Ni^{2+} sublattice will create charge disorder which will cause a distribution of EFGs at both sites leading to line broadening. The variable oxygen content — deficit or excess — is associated with changing concentrations of oxygen anions and changing amounts of Ni^{3+} and Ni^{2+} cations. This will also contribute to charge disorder in the lattice and, hence, contribute to line broadening in mixed crystals with $x > 0$ and $|\delta| > 0$. Thus, charge disorder — in addition to absorber thickness — explains the larger line widths for the sample with the higher dopant level, Table 2.

In an alternative explanation for the observation of two sites for Fe/Ni in $La_3Ni_{2-x}Fe_xO_{7\pm\delta}$, the possibility is to be

envisaged that a temperature-dependent reconstruction (intergrowth) of the Ruddlesden-Popper structure may occur. Locally, three perovskite-type layers of iron/nickel atoms may be formed, like in $La_4Ni_{3-x}Fe_xO_{10-\delta}$, which would provide two inequivalent sites for nickel (iron). With increasing temperatures, the local three-layer intergrowth (n = 3) could change to the higher symmetric n = 2 two-layer structure of $La_3Ni_2O_7$. Such a structural complexity could be a consequence of the fact that for the off-stoichiometric, iron-doped $La_3Ni_{2-x}Fe_xO_{7\pm\delta}$ ($\delta > 0$, $x > 0$) the number of Ni^{3+} and Ni^{2+} cations no longer obeys the ideal 1:1 ratio but, instead, is given by $[Ni^{3+}]:[Ni^{2+}] = 1 \mp (x \mp 4\delta)/(1 \mp 2\delta)$. In this context, it is also interesting to recall Mössbauer results reported for $La_4Ni_{3-x}Fe_xO_{10-\delta}$ with x = 0.03 [25]. Here, the two quadrupole doublets at RT show splittings of 0.43 $mm{\cdot}s^{-1}$ and 0.95 $mm{\cdot}s^{-1}$ which is very close to the RT *QS*-values observed for $La_3Ni_{2-x}Fe_xO_{7\pm\delta}$ in the present study, Table 2. However, the above scenario is difficult to accept in view of the fact that diffusional motion of all cations, La, Ni, and Fe, would be required for changing the local intergrowth situation. This conclusion is also supported by experience gathered by many authors in the (sluggish) high-temperature synthesis of $La_3Ni_2O_{7\pm\delta}$, see e. g. Refs. [7, 8, 11].

The discussion of the results from X-ray diffraction in Crystal structure section has led to the successful identification of several space groups which provide two nonequivalent sites for Ni/Fe in equal numbers. It must be admitted, however, that a final decision about the prevailing structure type could not be reached. Therefore, in the following another approach will be taken by considering the ^{57}Fe quadrupolar interactions at the two inequivalent sites in $La_3Ni_2O_7$. In this discussion it will be assumed that the electric field gradients at the iron nuclei, Eq. (1), arise from the so-called lattice contribution, $V_{\alpha\alpha}$(latt), i. e. from charges located on the ions surrounding the Mössbauer atom in the crystal lattice. Thus, the framework of the point charge model, the EFGs at the two sites for iron can be calculated in the principal axis system according to [29]:

$$V_{\alpha\alpha} = \left(1-\gamma_\infty\right) V_{\alpha\alpha}\left(latt\right) = \\ = \frac{e\left(1-\gamma_\infty\right)}{4\pi\varepsilon_0}\sum_i z_i\left(3\alpha_i^2 - r_i^2\right)r_i^{-5} \quad (3)$$

Here, the summation extends over the surrounding lattice ions of charge number z_i, and $(1 - \gamma_\infty)$ and ε_0 denote the Sternheimer factor and the vacuum permittivity, respectively. The lattice EFGs were calculated using the UNISOFT program package [39] and quadrupole splittings were obtained by using a Sternheimer factor for Fe^{3+} ions of $1 - \gamma_\infty = 10.42$ [40] and a quadrupole moment of $Q = 0.209{\cdot}10^{-28}$ m^2 [41].

In an approximation to the complex situation in real $La_3Ni_{2-x}Fe_xO_{7\pm\delta}$ solid solutions, the EFGs at the Ni1- and Ni2-sites have been calculated for an ideal rigid $La_3Ni_2O_7$ lattice (x = 0, δ = 0) employing the crystallographic RT data of $La_3Ni_2O_7$ obtained from the Rietveld refinements partially reported in Tables 5 and 6. In all cases, the assumption was made that the formal charge number of oxygen is –2. In the case of the *Fmmm* space group it was assumed that all Ni-sites are occupied by nickel cations possessing an average charge of +2.5 — corresponding to no charge ordering. For the lower-symmetric space groups, the two above defined cation distributions, (I) and (II), have been considered with charge numbers +2 for Ni^{2+} and +3 for Ni^{3+} and La^{3+}. Table 7 reports the results of these calculations according

to Eqs. (1) and (3). It is to be noted that the calculations neither account for Fe^{3+} cations introduced into the lattice by doping nor for possible deviations from exact stoichiometry. Because of their small numbers and their random distribution, it can be expected that the iron dopants and defects will not influence significantly the average electric field gradients at cation nickel sites, but will lead to a distribution of quadrupole interactions about the structure-determined averages.

As can be seen from Table 7 these admittedly simplistic point charge calculations, which also neglect lattice relaxation around the nuclear Fe probes and any effect of chemical bonding of the ferric cations, successfully yield ^{57}Fe quadrupole splittings of the right order of magnitude, i. e. $0.1 < QS/\mathrm{mm{\cdot}s^{-1}} < 1$.

Calculated quadrupole splittings in the orthorhombic space groups *Cmmm* and *Cmma*, Table 7, are in reasonable agreement with the experimental splittings of $QS(Fe_B) \approx 0.95$ mm·s^{-1} and $QS(Fe_A) \approx 0.45$ mm·s^{-1}, Table 2, for both types of cation distributions. However, calculated *QS*-values are always found smaller than experimental ones by about 20 %, Table 7. In view of the deficiencies of the point charge model in general and the simplifying assumptions made in the calculations, such deviations cannot be unexpected. In contrast, for orthorhombic *Bmmb* no acceptable agreement is observed between experiment and calculated values. In addition to consideration of the absolute values of quadrupolar interactions, special relevance is attributed to the ratio of splittings, $R_Q = QS(Fe_B)/QS(Fe_A)$, because of possible error cancellation in the calculations.

Table 7

Quadrupolar interactions in $La_3Ni_2O_7$: ^{57}Fe quadrupole splitting, *QS,* and splitting ratios R_Q, at the nickel sites of $La_3Ni_2O_7$ for space groups *Fmmm*, *Cmmm*, *Cmma*, and *Bmmb* and for the cation distributions, (I) and (II), which can be adopted by nickel in the lower symmetric structures. Calculations were performed in the framework of the point charge model according to Eqs. (1,3) with lattice parameters taken from respective Rietveld refinements

Space group	Cation distribution	Site	*QS* mm·s^{-1}	R_Q
Fmmm	—	Ni	0.74	—
Cmmm	(I)	Ni1	0.86	3.0
	(I)	Ni2	0.29	
	(II)	Ni1 / A	0.36	**2.2**
	(II)	Ni2 / B	0.79	
Cmma	(I)	Ni1 / B	0.81	**2.3**
	(I)	Ni2 / A	0.35	
	(II)	Ni1	0.28	3.1
	(II)	Ni2	0.88	
Bmmb	(I)	Ni1	0.83	1.1
	(I)	Ni2	0.75	
	(II)	Ni1	0.92	1.4
	(II)	Ni2	0.66	

At RT, the experimental ratio assumes values of about R_Q = 2.3 (x = 0.05) and R_Q = 2.0 (x = 0.10), Table 2. As can be seen from Table 7, such values are not consistent with those calculated for *Bmmb* where this ratio amounts to 1.1 or 1.4 for cation distributions (I) and (II), respectively. For *Cmmm*(I) as well as for *Cmma*(II) calculated ratios are significantly larger than the experimental R_Q-values. However, for *Cmmm*(II) and for *Cmma*(I) close agreement is observed with calculated ratios of 2.2 and 2.3, respectively, indicated in "bold" in Table 7. Because we see no further means for differentiation between the two structures, we arrive at the conclusion that space group *Cmmm* with a cation distribution of type (II) as well as space group *Cmma* with cation distribution (I) represent good structural models for $La_3Ni_{2-x}Fe_xO_{7\pm\delta}$ solid solutions at RT.

In the present combined approach involving diffraction and spectroscopic work, A- and B-sites can be even be assigned to the Ni1- and Ni2-sites in these space groups according to the quadrupole splittings calculated for the respective types of cation distribution, see Table 7. This conclusion on the crystal structure of $La_3Ni_{2-x}Fe_xO_{7\pm\delta}$, which is in agreement with the space groups arrived at on the basis of general structural considerations and Rietveld refinements of the materials, narrows down considerably the number of possible combinations of space groups and cation distributions of $La_3Ni_{2-x}Fe_xO_{7\pm\delta}$ at RT.

Conclusions

At RT, local probe ^{57}Fe Mössbauer spectroscopy has provided indisputable evidence for the existence of two non-equivalent sites for Fe^{3+} in $La_3Ni_{2-x}Fe_xO_{7\pm\delta}$ with site populations closely corresponding to the 1:1 ratio. This unexpected result is in contrast to the hitherto existing structure determinations of $La_3Ni_2O_{7\pm\delta}$. The latter assumed space groups *Fmmm* or *Cmcm* (*Amam*) which both provide only a single unique site for nickel/iron. In view of the spectroscopic findings, the RT structure of $La_3Ni_{2-x}Fe_xO_{7\pm\delta}$ has been reconsidered and X-ray diffraction patterns for samples with x = 0, 0.05, and 0.10 have been measured and refined by the Rietveld method. The interest was in the identification of alternative structural models which could replace the previously used space groups. From general considerations, we have selected the orthorhombic space groups *Cmma*, *Cmmm*, and *Bmmb* which fulfill the spectroscopic requirements of providing two sites in equal numbers for Ni/F. According to Rietveld refinements, *Cmma* and *Cmmm* can be considered the preferred space groups. Calculations of the quadrupolar interactions at the iron nuclei in $La_3Ni_2O_7$ in the framework of the point charge model have confirmed this conclusion and provided additional information on the specific distribution of Ni^{2+} and Ni^{3+} cations in these structures at RT.

Acknowledgements

K.-D.B. and P.G. would like to thank the Volkswagen-Foundation and the State of Lower Saxony (Germany) for financial support of the present work. E.K. and V.C. acknowledge support of their work by the Ministry of Education and Science of the Russian Federation. A.F. is grateful to the Deutsche Forschungsgemeinschaft (DFG) for financial support in the frame of grant FE928/7–1. Thanks are also due to Prof. Th. Gesing

(U Bremen, Germany) for chemical EDX analyses of samples. E.K and V. Ch. work was supported by Act 211 Government of the Russian Federation, agreement 02.A03.21.0006.

References

1. Amow G, Davidson IJ, Skinner SJ. A comparative study of the Ruddlesden-Popper series, $La_{n+1}Ni_nO_{3n+1}$ (n = 1, 2 and 3), for solid-oxide fuel-cell cathode applications. Solid State Ionics. 2006;177(13–14):1205–10.
   DOI: 10.1016/j.ssi.2006.05.005.
2. Goettler R, Xing Z, Xue L, Hill M. Evaluation of Ruddlesden-Popper nickelate cathodes for higher temperature SOFC. Ceramic Engineering and Science Proceedings. 2008;28(4):183–94.
   DOI: 10.1002/9780470339534.ch18.
3. Takahashi S, Nishimoto S, Matsuda M, Miyake M, Electrode properties of the Ruddlesden–Popper series, $La_{n+1}Ni_nO_{3n+1}$ (n= 1, 2, and 3), as intermediate-temperature solid oxide fuel cells. J. Am. Ceram. Soc. 2010;93(8):2329–33.
   DOI: 10.1111/j.1551–2916.2010.03743.x.
4. Woolley RJ, Skinner SJ. Novel $La_2NiO_{4+\delta}$ and $La_4Ni_3O_{10-\delta}$ composites for solid oxide fuel cell cathodes. J. Power Sources. 2013;243:790–95.
   DOI: 10.1016/j.jpowsour.2013.06.106.
5. Woolley RJ, Skinner SJ. Functionally graded composite $La_2NiO_{4+\delta}$ and $La_4Ni_3O_{10-\delta}$ solid oxide fuel cell cathodes. Solid State Ionics. 2014;255:1–5.
   DOI: 10.1016/j.ssi.2013.11.041.
6. Brisi C., Vallino M, Abbattista F. Composition and structure of two hitherto unidentified phases in the system La_2O_3-NiO-O. J. Less Common Metals, 1981;79(2): 215–19.
   DOI: 10.1016/0022–5088(81)90070–9.
7. Drennan J, Tavares CP, Steele BCH. An electron microscope investigation of phases in the system La–Ni–O. Mat. Res. Bull. 1981;17(5):621–26.
   DOI: 10.1016/0025–5408(82)90044–7.
8. Odier P, Nigara Y, Coutures J, Sayer M. Phase relations in the La–Ni–O system: Influence of temperature and stoichiometry on the structure of La_2NiO_4. J. Solid State Chem. 1985;56(1):32–40.
   DOI: 10.1016/0022–4596(85)90249-X.
9. Ram RM, Ganapathi L, Ganguly P, Rao CNR. Evolution of three-dimensional character across the $La_{n+1}Ni_nO_{3n+1}$ homologous series with increase in n. J. Solid State Chem. 1986;63(2):139–47.
   DOI: 10.1016/0022–4596(86)90163–5.
10. Sreedhar K, McElfresh M, Perry D, Kim D, Metcalf P, Honig JM. Low-temperature electronic properties of the $La_{n+1}Ni_nO_{3n+1}$ (n = 2, 3, and∞) system: evidence for a crossover from fluctuating-valence to Fermi-liquid-like behavior. J. Solid State Chem. 1994;110(2):208–15.
    DOI: 10.1006/jssc.1994.1161.

11. Zhang Z, Greenblatt M, Goodenough JB. Synthesis, structure, and properties of the layered perovskite $La_3Ni_2O_{7-\delta}$. J. Solid State Chem. 1994;108(2):402–09. DOI: 10.1006/jssc.1994.1059.
12. Carvalho MD, Costa FMA, Pereira IS, Wattiaux A, Bassat JM, Grenier JC, Pouchard M. New preparation method of $La_{n+1}Ni_nO_{3n+1-\delta}$ (n= 2, 3). J. Mater. Chem. 1997;7(10):2107–11. DOI: 10.1039/A702424J.
13. Sasaki H, Harashina H, Taniguchi S, Kasai M, Kobayashi Y, Sato M, Sakata M. Structural studies on the phase transition of $La_3Ni_2O_{6.92}$ at about 550, K. J. Phys. Soc. Jpn. 1997;66(6):1693–97. DOI: 10.1143/jpsj.66.1693.
14. Ling CD, Argyriou DN, Wu G, Neumeier JJ. Neutron diffraction study of $La_3Ni_2O_7$: Structural relationships among n = 1, 2, and 3 phases $La_{n+1}Ni_nO_{3n+1}$. J. Solid State Chem. 2000;152(2):517–25. DOI: 10.1006/jssc.2000.8721.
15. Voronin VI, Berger IF, Cherepanov VA, Gavrilova LY, Petrov AN, Ancharov AI, Nikitenko SG. Neutron diffraction, synchrotron radiation and EXAFS spectroscopy study of crystal structure peculiarities of the lanthanum nickelates $La_{n+1}Ni_nO_y$ (n = 1, 2, 3). Nucl. Instrum. Methods Phys. Res., Sect. A. 2001;470(1–2):202–209. DOI: 10.1016/S0168–9002(01)01036–1.
16. Bannikov DO, Cherepanov VA. Thermodynamic properties of complex oxides in the La–Ni–O system. J. Solid State Chem. 2006;179(8):2721–27. DOI: 10.1016/j.jssc.2006.05.026.
17. Savchenko VF, Ivashkevich LS,. Lubkina IYa, Russ. J. Inorg. Chem. 1988;33:30–33.
18. Kobayashi Y, Taniguchi S, Kasai M, Sato M, Nishioka, Kontani M. Transport and magnetic properties of $La_3Ni_2O_{7-\delta}$ and $La_4Ni_3O_{10-\delta}$. J. Phys. Soc. Jpn. 1996;65(12):3978–82. DOI: DOI.org/10.1143/jpsj.65.3978.
19. Gervais F, Odier P, Nigara Y. Plasmon behavior at the "semiconductor-metal" transition in La_2NiO_4 and $La_3Ni_2O_7$. Solid State Commun. 1985;56(4):371–74. DOI: 10.1016/0038–1098(85)90405–3.
20. Zinkevich M, Solak N, Nitsche H, Ahrens M, Aldinger F. Stability and thermodynamic functions of lanthanum nickelates. J. Alloys Compd. 2007; 438(1–2):92–99. DOI: 10.1016/j.jallcom.2006.08.047.
21. Fontcuberta J, Longworth G, Goodenough JB. Magnetic order or charge-density wave in La_2NiO_4 by Mössbauer spectroscopy. Phys. Rev. B. 1984;30(11):6320. DOI: 10.1103/PhysRevB.30.6320.
22. Tsipis EV, Naumovich EN, Patrakeev MV, Waerenborgh JC, Pivak YV, Gaczyński P, Kharton VV. Oxygen non-stoichiometry and defect thermodynamics in $La_2Ni_{0.9}Fe_{0.1}O_{4+\delta}$. J. Phys. Chem. Solids. 2007;68(7):1443–55. DOI: 10.1016/j.jpcs.2007.04.006.
23. Klande T, Efimov K, Cusenza S, Becker KD, Feldhoff A. Effect of doping, microstructure, and CO_2 on $La_2NiO_{4+\delta}$-based oxygen-transporting materials. J. Solid State Chem. 2011;184(12):3310–18. DOI: 10.1016/j.jssc.2011.10.019.

24. Klande T, Cusenza S, Gaczyński P, Becker KD, Dörrer L, Borchardt G, Feldhoff A. In-situ Mössbauer studies of ^{57}Fe-doped Ruddlesden–Popper type lanthanum nickel oxides. Solid State Ionics, 2012;222–223:8–15.
DOI: 10.1016/j.ssi.2012.06.019.
25. Carvalho MD, Wattiaux A, Ferreira LP, Bassat JM. Mössbauer investigation of ^{57}Fe doped $La_4Ni_3O_{10\pm y}$ phases. J. Solid State Chem. 2009;182(1):60–64.
DOI: 10.1016/j.jssc.2008.10.006.
26. Tsipis EV, Patrakeev MV, Waerenborgh JC, Pivak YV, Markov AA, Gaczyński P, Kharton VV. Oxygen non-stoichiometry of $Ln_4Ni_{2.7}Fe_{0.3}O_{10-\delta}$ (Ln = La, Pr). J. Solid State Chem. 2007;180(6):1902–10.
DOI: 10.1016/j.jssc.2007.04.025.
27. Rodriguez-Carvajal J. Commission on powder diffraction (IUCr). Newsletter, 2001;26:12.
28. Lagarec K, Rancourt DG. RECOIL, Mössbauer spectral analysis software for windows (version 1.02). Ottawa: Department of Physics, University of Ottawa;1998.
29. Gütlich P, Bill E, Trautwein AX. Mössbauer Spectroscopy and Transition Metal Chemistry. Berlin, Heidelberg: Springer; 2011. 568 p.
DOI: 10.1007/978–3–540–88428–6.
30. Menil F. Systematic trends of the ^{57}Fe Mössbauer isomer shifts in (FeO_n) and (FeF_n) polyhedra. Evidence of a new correlation between the isomer shift and the inductive effect of the competing bond TX (→ Fe)(where X is O or F and T any element with a formal positive charge). J. Phys. Chem. Solids. 1985;46(7):763–89.
DOI: 10.1016/0022–3697(85)90001–0.
31. Rancourt DG. Accurate site populations from Mössbauer spectroscopy. Nucl. Instrum. Methods Phys. Res., Sect. B. 1989;44(2):199–210.
DOI: 10.1016/0168–583X(89)90428-X.
32. Boultif A, Louër D. Powder pattern indexing with the dichotomy method. J. Appl. Crystallogr. 2004;37(5):724–31
DOI: 10.1107/S0021889804014876.
33. Visser JW. A fully automatic program for finding the unit cell from powder data. J. Appl. Crystallogr. 1969;2(3):89–95.
DOI: 10.1107/S0021889869006649.
34. Roisnel T, Rodríquez-Carvajal J. WinPLOTR: a windows tool for powder diffraction pattern analysis. In Materials Science Forum (Vol. 378, No. 1, pp. 118–123). Transtec Publications, 1999.
35. Hahn Th. International Tables for Crystallography, Vol. A: Space-group symmetry. 5th ed. Dordrecht: Springer, 2005. 911 p.
36. Kraus W, Nolze G. POWDER CELL-a program for the representation and manipulation of crystal structures and calculation of the resulting X-ray powder patterns. J. Appl. Crystallogr. 1996;29(3):301–03.
DOI: 10.1107/S0021889895014920.
37. Shannon RD. Revised effective ionic radii and systematic studies of interatomic distances in halides and chalcogenides. Acta Cryst. 1976; A32:751–67.
DOI: 10.1107/S0567739476001551.

38. Taniguchi S, Nishikawa T, Yasui Y, Kobayashi Y, Takeda J, Shamoto SI, Sato M. Transport, magnetic and thermal properties of $La_3Ni_2O_{7-\delta}$. J. Phys. Soc. Jpn. 1995;64(5):1644–50.
DOI: DOI.org/10.1143/jpsj.64.1644.
39. Eckold G. UNISOFT — A Program Package for Lattice-Dynamical Calculations: User Manual, 2nd rev. ed. Jülich: Jülich Forschungszentrum, 1992.
40. Stevens JG, Dunlap BD. Nuclear moments and moment ratios as determined by Mössbauer spectroscopy. J. Phys. Chem. Ref. Data, 1976;5(4):1093–122.
DOI: 10.1063/1.555541.
41. Liverts EZ, Zhetbaev AK. Sternheimer Quadrupole Factors in Ferric Compounds. Phys. Status Solidi B. 1982;111(2):469–475.
DOI: 10.1002/pssb.2221110207.

Please note that all new submissions will be accepted in English only. Requirements for the manuscript preparation are available on the Journal's website and in the following template

Chimica Techno Acta manusctipt style guidelines (title)

A.N. Authorname[a], A.N. Authorname[b], A.N. Authorname[ab]

[a] Institution, address, city, country

[b] Institution, address, city, country

e-mail: corresponding_author@e-mail.com

Abstract

The abstract should be a single paragraph (up to 300 words) in plain text (that means — no formulae or references are permitted) that summarises the content of the article. It should set the main objectives and results of the work; giving the reader a clear idea of what has been achieved. An abstract should not be extremely short though — if yours is 1–2 sentences long, then you're not doing it right. Make sure that you use well-known, searchable terms and phrases.

Keywords: short; searchable; keywords (up to 10).

Introduction

An introduction should 'set the scene' of the work. It should clearly explain both the nature of the problem under investigation and its background. It should start off general and then focus in to the specific research question you are investigating. Ensure you include all relevant references.

Experimental (if appropiate)

Descriptions of the experiments should be provided in enough detail so that a skilled researcher is able to repeat them. Methods already published or experimental techniques already described elsewhere should be indicated by a reference. Only non-standard apparatus should be described in details; commercially available instruments are referred to by their stock numbers.

Results and discussion

This is undoubtedly the most important section of your article. It should consist of the logically ordered sequence of text, formulae, images and tables.

All formulae which appear in their own line should be numbered:

$$A = B + C \tag{1}$$

Tables should be used only when they can present information more efficiently than running text or even an image:

Table 1

Just an ordinary table without any sophisticated formatting applied

A	B	C	D
1	2	3	4
+	+	+	–

All illustrations should be of a high quality (300 dpi or higher) and should be placed in the flow of the text, not in the end of an article:

Fig. 1. Just an ordinary image

Please bear in mind that all illustrations and tables should fit smoothly within either single column (approx. 6 cm) or double column (approx. 12 cm) width.

Conclusions

Your conclusions should summarize the main paper, underline the interpretation of the key results and highlight the novelty and significance of the work. They may address some plans for relevant future work as well.

Acknowledgements (if appropiate)

All sources of funding such as grants should be declared here. Individuals who contributed to the research but are not co-authors may also be briefly acknowledged.

References

A reference should be indicated in square brackets in line with the text (e.g. [1]). The actual references in the reference list should be numbered in the order in which they appear in the text. In Chimica Techno Acta so-called Vancouver Citation Style is adopted almost as it is described in the following public domain textbook [1]:

1. Patrias K. Citing medicine: the NLM style guide for authors, editors, and publishers [Internet]. 2nd ed. Wendling DL, technical editor. Bethesda (MD): National Library of Medicine (US); 2007- [updated 2015 Oct 2; cited 2017 Jun 07]. Available from: http://www.nlm.nih.gov/citingmedicine

Note that opposed to [1] we omit the date of publication (leaving year only) of the referenced journal article, as almost all journals are continuously paginated throughout the volume. And another one — DOI or a hyperlink should always come last in a reference. These are the only major differences between our style and such described in [1], so when in doubt — you can always refer to [1], it contains tremendous number of well-organized examples.

For your convenience, below are some references to the different types of publications:

Books

2. Livingstone S. The Chemistry of Ruthenium, Rhodium, Palladium, Osmium, Iridium and Platinum. Oxford: Pergamon; 1973. 222 p.

3. Bard AJ, Faulkner LR. Electrochemical Methods: Fundamentals and Applications. 2nd ed. New York: John Wiley & Sons; 2001. 833 p.

Books not in English

4. Evdokimov AA, Efremov VA, Trunov VK, Kleyman IA, Tananaev IV. Soedineniya redkozemel'nykh elementov. Molibdaty, vol'framaty [Rare-earth elements' compounds. Molibdates, wolframates]. Moscow: Nauka; 1991. 267 p. Russian.

* Translation of the title in square brackets is not required, but highly desirable.

* For Cyrillic languages, such as Russian, please use consistent transliteration system. There are plenty, but we strongly recommend BGN/PCGN Romanization as it's one of the

easiest to read and implement (https://en.wikipedia.org/wiki/BGN/PCGN_romanization_of_Russian).

Journal articles

5. Zuev AYu, Tsvetkov DS. Oxygen nonstoichiometry, defect structure and defect-induced expansion of undoped perovskite $LaMnO_{3\pm\delta}$. Solid State Ionics. 2010;81(11–12):557–63. DOI:10.1016/j.ssi.2010.02.024

6. Shannon RD. Revised effective ionic radii and systematic studies of interatomic distances in halides and chalcogenides. Acta Cryst. 1976;A32:751–67. DOI:10.1107/S0567739476001551

7. Allred AL, Rochow EG. A scale of electronegativity based on electrostatic force. J Inorg Nucl Chem. 1958;5(4):264–8. DOI:10.1016/0022-1902(58)80003-2

* For the majority of chemical journals corresponding abbreviation is defined in Chemical Abstracts Service Source Index (CASSI, http://cassi.cas.org). If an abbreviation is not available there, please use the full name of a journal.

* Note that DOI of an article, when available, should always be provided.

Journal articles on the Internet (e.g. for online-only journals without DOI)

8. Tkach V, Nechyporuk V, Yagodynets P. Descripción matemática de la síntesis electroquímica de polímeros conductores en la presencia de surfactants. Avances en Química [Internet]. 2013[cited 2016];8(1):9–15. Spanish. Available from: http://erevistas.saber.ula.ve/index.php/avancesenquimica/article/download/6357/6168

Conference abstracts

9. Zuev AYu, Sereda VV, Malyshkin DA, Ivanov IL, Tsvetkov DS. Mechano-chemical coupling in double perovskites as energy related materials. In: Abstracts of the XX Mendeleev Congress on general and applied chemistry, Vol. 3; 2016 Sep 26–30; Ekaterinburg, Russia. p. 325.

10. Steparuk AS, Usachev SA, Tsvetkov DS, Sosnovskikh VYa, Zuev AYu. Novyy katodnyy material na osnove mayenita dlya elektrokhimicheskogo karboksilirovaniya organicheskikh soedineniy [New mayenite-based cathode material for electrochemical carboxylation of organic compounds]. In: Tezisy dokladov XXVI Rossiyskoy molodezhnoy nauchnoy konferentsii "Problemy teoreticheskoy i eksperimental'noy khimii" [Abstracts of XXVI Russian scientific conference for young scientists "Problems of theoretical and experimental chemistry"]; 2016 Apr 27–29; Ekaterinburg, Russia. p. 285–286. Russian.

Dissertations

11. ten Donkelaar SFP. Development of Stable Oxygen Transport Membranes [dissertation]. Enschede (The Netherlands): University of Twente; 2015. 140 p.

Patents

12. Chemezov OV, Batukhtin VP, Apisarov AP, Isakov AV, Zaikov YuP, inventors; Institute of High-Temperature Electrochemistry UB RAS, assignee. Sposob polucheniya nano- i mikrovolokon kremniya elektrolizom dioksida kremniya iz rasplavov soley. Russian Federation patent RU 2427526. 2011 Aug 27. Russian.

13. Menta E, Da Re G, Grugni M., authors; Cti Europe S.R.L., assignee. Derivatives of chromen-2-one as inhibitors of vegf production in mammalian cells. United States patent US20060122387 A1. 2006 Jun 8.

Chimica Techno Acta
© Уральский федеральный университет, 2019

Редакционный совет
Главный редактор
А. Ю. Зуев (Екатеринбург, Россия)
Зав. редакцией
Т. А. Поспелова (Екатеринбург, Россия)
Научный редактор
В. В. Середа (Екатеринбург, Россия)
Редакторы
Е. В. Антипов (Москва, Россия)
В. А. Черепанов (Екатеринбург, Россия)
Ж.-Дж. Фан (Тяньцзинь, Китай)
В. В. Гусаров (Санкт-Петербург, Россия)
В. В. Хартон (Черноголовка, Россия)
А. А. Михайловский (Санта-Барбара, США)
В. В. Паньков (Минск, Беларусь)
Согата Сантра (Екатеринбург, Россия)
Н. В. Таракина (Берлин, Германия)
Г. В. Зырянов (Екатеринбург, Россия)
Д. А. Медведев (Екатеринбург, Россия)
П. Циакарас (Фессалия, Греция)
С. Сонг (Гуанчжоу, Китай)
Й. Ванг (Гуанчжоу, Китай)

Учредитель —
Уральский федеральный университет
имени первого Президента России Б. Н. Ельцина
620002, Россия, Екатеринбург, ул. Мира, 19

Свидетельство о регистрации
ПИ № ФС77-56172 от 15.11.2013

Адрес журнала:
Россия, 620000,
Екатеринбург, ул. Мира, 28, оф. Х-268
E-mail: t.a.pospelova@urfu.ru

Формат 70×100/16. Тираж 500 экз. Заказ № 261.

Отпечатано в типографии
Издательско-полиграфического центра УрФУ
620000, Екатеринбург, ул. Тургенева, 4
Тел.: +7 (343) 350-56-64, 350-90-13
Факс: +7 (343) 358-93-06
E-mail: press-urfu@mail.ru

Editorial Board
Editor-in-Chief
A. Yu. Zuev (Ekaterinburg, Russia)
Managing Editor
T. A. Pospelova (Ekaterinburg, Russia)
Copyeditor
V. V. Sereda (Ekaterinburg, Russia)
Editors
E. V. Antipov (Moscow, Russia)
V. A. Cherepanov (Ekaterinburg, Russia)
Zh.-J. Fan (Tianjin, China)
V. V. Gusarov (Saint Petersburg, Russia)
V. V. Kharton (Chernogolovka, Russia)
A. A. Mikhailovsky (Santa Barbara, United States)
V. V. Pankov (Minsk, Belarus)
Sougata Santra (Ekaterinburg, Russia)
N. V. Tarakina (Berlin, Germany)
G. V. Zyryanov (Ekaterinburg, Russia)
D. A. Medvedev (Ekaterinburg, Russia)
P. Tsiakaras (Thessaly, Greece)
S. Song (Guangzhou, China)
Y. Wang (Guangzhou, China)

Founded by Ural Federal University named after
the first President of Russia B. N. Yeltsin
19, Mira St., Ekaterinburg, 620002, Russia

Journal Registration Certificate
PI № FS 77-56172 as of 15.11.2013

Principal Contact
Office X-268, Mira Str.,
620000, Ekaterinburg, Russia
E-mail: t.a.pospelova@urfu.ru

Format 70×100/16.
Circulation 500 cop.

Publisher — Ural Federal University
Publishing Centre
4, Turgenev St., 620000 Ekaterinburg, Russia
Phone: +7 343 350 56 64, +7 343 350 90 13
Fax: +7 343 358 93 06
E-mail: press-urfu@mail.ru

© Ural Federal University,
2019